CAS FGOALS-f3-L large-ensemble simulations for the CMIP6 Polar Amplification Model Intercomparison Project

Bian HE[1,2,3], Xiaoqi ZHANG[4,1], Anmin DUAN[1,2,3], Qing BAO[1], Yimin LIU[1,2,3], Wenting HU[1], Jinxiao LI[1], Guoxiong WU[1,3]

[1]State Key Laboratory of Numerical Modeling for Atmospheric Sciences and Geophysical Fluid Dynamics (LASG), Institute of Atmospheric Physics (IAP), Chinese Academy of Sciences, Beijing, 100029, China

[2]CAS Center for Excellence in Tibetan Plateau Earth Sciences, Beijing 100101, China

[3]University of Chinese Academy of Sciences, Beijing 100029, China

[4]School of Atmospheric Sciences, Nanjing University of Information Science and Technology, Nanjing 210044, China

Corresponding author: Bian He, heb@lasg.iap.ac.cn

ORCID: 0000-0002-7290-2201

Submition to Journal of Advances in Modeling Earth Systems

Special issue: The Chinese Academy of Sciences Climate and Earth System Models (CAS-FGOALS and CAS-ESM) and Applications

Abstract

Large-ensemble simulations of the atmosphere-only time-slice experiments for the Polar Amplification Model Intercomparison Project (PAMIP) were carried out by the model group of the Chinese Academy of Sciences (CAS) Flexible Global Ocean-Atmosphere-Land System (FGOALS-f3-L). Eight groups of experiments forced by different combinations of the sea surface temperature (SST) and sea ice concentration (SIC) for pre-industrial, present-day and future conditions were performed and submitted. The time-lag method was used to generate the 100 ensemble members, with each member integrating from 1st April 2000 to 30th June 2001 and the first two months as the spin-up period. The basic model responses of the surface air temperature (SAT) and precipitation were documented. The results indicate that Arctic amplification is mainly caused by Arctic SIC forcing changes. The SAT responses to the Arctic SIC forcing alone show an obvious meridional gradient over high latitudes, which is similar to the results from the combined forcing of SST and SIC. However, the change in global precipitation is dominated by the changes in the global SST rather than SIC, partly because tropical precipitation is mainly driven by local SST changes. The uncertainty of the model responses was also investigated through the analysis of the large-ensemble members. The relative roles of SST and SIC, together with their combined influence on Arctic amplification, are also discussed. All these model datasets will contribute to PAMIP multimodel analysis and improve the understanding of polar amplification.

Key words: Polar amplification, PAMIP, large-ensemble simulation, sea ice, FGOALS-f3-L, CMIP6

Plain Language Summary

Polar amplification is the most prominent phenomenon under global warming featured by the surface air temperature increased rapidly in polar region during recent decades. The cause and effect of polar amplification remains debate due to climate model uncertainties. In this study, the CAS FGOALS-f3-L provided large-ensemble simulations for the CMIP6 PAMIP Tier-1 projection with eight groups of atmosphere-only time-slice experiments for understanding the model responses to the different combinations of global SST and SIC forcing under pre-industrial, present-day and future condition. Each group contains 100 ensemble members. The results suggested that the Arctic amplification is dominantly controlled by changes in the Arctic SIC. The SAT responses to the Arctic SIC changes show an obvious meridional gradient over high latitudes, which is similar to the results from the combined forcing of SST and SIC. However, the changes in global precipitation for the present day are dominated by the changes in the global SST relative to the changes in SIC, partly because tropical precipitation is mainly driven by local SST forcing. The future model response is similar overall to the present-day response; in particular, the future response is stronger than the present-day response due to the larger forcing changes.

1. Introduction

Polar amplification is a phenomenon in which the surface air temperature (SAT) changes at high latitudes exceed the globally averaged SAT changes in response to climate forcing, such as the rapid increase in greenhouse gases (GHGs) during the 20th century. Observational studies (Serreze et al. 2009; Screen and Simmonds 2010; Cowtan and Way 2013, IPCC, 2013) reveal that the Arctic has warmed at a rate of 1.36 °C per century since 1875, approximately twice as fast as the global average, and that since 1979, the Arctic land surface has warmed at an even higher rate of 0.5 °C per decade. Specifically, the surface temperatures have increased up to 3 °C in parts of northern Alaska (early 1980s to mid-2000s) and up to 2 °C in parts of Russia's European North (1971 to 2010); these values are 2 to 3 times greater than the average warming experienced globally. This prominent phenomenon is accompanied by the continuous melting of ice. As documented in the Intergovernmental Panel on Climate Change Fifth Assessment Report (IPCC AR5) (IPCC, 2013), the annual mean Arctic sea ice extent decreased by 3.5 to 4.1% per decade from 1979 to 2012, and this decrease was most rapid in summer and autumn.

The cause of polar amplification is the topic of many scientific studies and remains debated. The most popular mechanism proposed is surface albedo feedback (Manabe and Stouffer, 1994; Holland and Bitz, 2003; Hall, 2004; Screen and Simmonds, 2010; Screen et al., 2012; Taylor et al., 2013; Stuecker et al., 2018; Dai et al., 2019; Curry et al., 1995; Serreze and Barry, 2011). The decline in sea ice in the Arctic leads to a decrease in sea surface albedo *in situ*, allowing the sea surface to absorb more solar radiation. Then, the sea surface warms, causing more sea ice loss and thus a positive feedback cycle. However, some studies have argued that the lapse rate and Planck (longwave) feedbacks are more important than surface albedo feedback (Manabe and Wetherald, 1975; Winton, 2006; Bintanja et al., 2012; Pithan and Mauritsen, 2014; Goosse et al., 2018) because Arctic amplification also occurred in experiments without changes in snow and ice cover (Hall, 2004; Graversen, 2009). Moreover, other studies have emphasized the contributions of water vapor feedback (Manabe and Wetherald, 1980; Graversen and Wang, 2009; Lu and Cai, 2009; Gao et al., 2019), cloud feedback (Holland and Bitz, 2003; Vavrus, 2004; Abbot and Tziperman, 2008), and atmospheric and oceanic heat transport (Khodri et al., 2001; Spielhagen et al., 2011) to Arctic amplification.

The influence of polar amplification is another often-investigated topic that has already been addressed in many scientific studies. A number of recent studies (Cohen et al., 2014; Walsh, 2014; Vihma, 2014; Overland et al., 2015; Barnes and Screen, 2015; Gramling, 2015; Shepherd, 2016; Screen, 2017; Sévellec et al., 2017; Zhang et al., 2018) revealed that Arctic amplification could influence the weather and climate in the Northern Hemisphere through both atmospheric circulation anomaly and oceanic circulation changes. The air over the Arctic perturbed by the sea ice loss and warm surface is advected to lower latitudes, which could impact weather and climate systems such as the westerly jet, Aleutian Low, and Siberian High, thus inducing extreme weather events in the mid-latitudes. For example, the recently observed Warm Arctic, Cold Continents pattern is considered to be a climatic response to Arctic amplification (Liu et al. 2012; Mori et al. 2014; 5 Kretschmer et al. 2017; Overland et al. 2011; Cohen et al. 2013; Zhang et al., 2018; Xie et al. 2020). Arctic warming could also reduce the meridional temperature gradient over the Northern Hemisphere and influence the natural variability of the Arctic Oscillation (AO) and North Atlantic Oscillation (NAO) (Magnusdottir et al., 2004; Seierstad and Bader, 2009; Screen et al., 2014; Cassano et al., 2014).

Although extensive studies have investigated different aspects of the causes and effects of polar amplification, the understanding of this phenomenon remains debate, which can be mainly attributed to the different climate model behaviors in response to identical external forcing (Serreze and Francis, 2006; Shepherd, 2016; Screen et al., 2018). To reduce the uncertainties in the simulation of polar amplification and improve our understanding of the physical processes that drive this process and its global impacts, Smith et al. (2018) coordinated the Polar Amplification Model Intercomparison Project (PAMIP) as one of the endorsed MIPs during the six phases of the Coupled Model Intercomparison Project (CMIP6) (Eyring et al., 2016).

The PAMIP is designed to address two questions (Smith et al., 2018): 1. What are the relative roles of local sea ice and remote sea surface temperature (SST) changes in driving polar amplification? 2. How does the global climate system respond to changes in Arctic and Antarctic sea ice? These questions can be addressed by comparing numerical model simulations forced with different combinations of SST and/or sea ice concentration (SIC). To reduce the simulation uncertainty, the PAMIP requires the participating model group to conduct a large-ensemble simulation with at

least 100 ensemble members for each experiment to obtain statistically robust results since models typically simulate a small atmospheric response to sea ice relative to the internal variability (Screen et al. 2014; Mori et al. 2014). Furthermore, the large-ensemble simulation will effectively reduce the model error from the model initialization and model random errors.

A low-resolution version of the Chinese Academy of Sciences (CAS) Flexible Global Ocean-Atmosphere-Land System Model, finite-volume version 3 (CAS FGOALS-f3-L), climate system model (Bao and Li, 2020) was developed at the State Key Laboratory of Numerical Modeling for Atmospheric Sciences and Geophysical Fluid Dynamics (LASG), Institute of Atmospheric Physics (IAP), CAS. The model group has carried out atmosphere-only time-slice experiments for the PAMIP and published the model datasets on the Earth System Grid Federation (ESGF) website since November 2019. These experiments aim to investigate the relative effects of SST and SIC in the Arctic and Antarctic on global climate change under both historical and future conditions. These experiments will complement the large-ensemble simulations of the PAMIP to facilitate the understanding of the mechanisms of polar amplification and to reduce the uncertainties in projections of future polar climate change and the associated impacts. They will also be helpful for examining the modeled climate responses and providing useful information for model development.

The goal of this paper is to provide a description of the PAMIP experiments produced by CAS FGOALS-f3-L and the relevant essential model configurations and experimental methods for a variety of users. A preliminary evaluation of the model responses of the global SAT and precipitation is also documented in a broad sense. The following paragraphs are organized as follows: Section 2 presents a description of the model and experimental design. Section 3 addresses the large-ensemble simulations of SAT and precipitation for all the experiments. Section 4 provides the final conclusions and discussion.

2. Model and experimental design

2.1 Introduction to the Model

CAS FGOALS-f3-L is a climate system model developed at LASG/IAP. The model contains five components, including an atmospheric model, a land model, an

oceanic model, a sea ice model and a coupler. Detailed descriptions of each component and basic performances for the CMIP6 DECK and historical experiments are documented in He et al. (2020) and Guo et al. (2020). Because the atmosphere-only time-slice experiments in the PAMIP were performed by the model group, the dynamical core and model physics of the atmospheric component are introduced in this section.

The atmospheric model in CAS FGOALS-f3-L is version 2.2 of the Finite-volume Atmospheric Model (FAMIL) (Zhou et al., 2015; Bao et al., 2018; He et al., 2019). The finite-volume dynamical core (Lin, 2004) on a cubed-sphere grid (Putman and Lin, 2007) is applied in FAMIL. The horizontal resolution is approximately equal to 1°×1° after remapping from the native grids. The vertical hybrid coordinate is 32 layers with the model top at 2.16 hPa. The atmospheric boundary layer employs a moisture turbulence scheme (Bretherton and Park, 2009), with updated shallow convection (Wang and Zhang, 2014). The Geophysical Fluid Dynamics Laboratory (GFDL) version of a single-moment six-category cloud microphysics scheme is used (Lin et al., 1983, Harris and Lin, 2014). For the cloud macrophysics, the Xu and Randall (1996) scheme is used, which considers not only relative humidity but also the cloud mixing ratio. Resolving convective precipitation parameterization (Bao and Li, 2019) is used, where, in contrast to conventional convective parameterization, convective and stratiform precipitation are calculated explicitly. The radiation scheme is from the Rapid Radiative Transfer Model for GCMs (RRTMG) (Clough et al., 2005), which utilizes the correlated k-distribution technique to efficiently calculate the irradiance and heating rate on the basis of 14 shortwave and 16 longwave spectral intervals. The model also applies a gravity wave drag scheme based on Palmer et al. (1986). The FAMIL version fixed for CMIP6 experiments can capture the basic performance of global climate systems well and is especially good at providing simulations of intraseasonal oscillation (ISO) and tropical cyclones (He et al., 2019; Li et al., 2019) compared with the last version for CMIP5 (Bao et al., 2013).

2.2 Experimental design

Atmosphere-only time-slice experiments from No. 1.1 to 1.8 (Table 1 in Smith et al., 2018) in the PAMIP were carried out based on CAS FGOALS-f3-L (Table 1).

These experiments use different combinations of SST and SIC representing present-day (pd), pre-industrial (pi) and future (fut, representing 2-degree warming) conditions. The present-day SST (pdSST) and SIC (pdSIC) were acquired from the 1979-2008 mean Hadley Centre Ice and Sea Surface Temperature dataset (HadISST, Rayner et al. 2003). The pre-industrial SST (piSST) and SIC (piSIC) were obtained from an ensemble of 31 historical CMIP5 model outputs but by removing an estimated global warming index (Haustein et al. 2017) for the period of 1979-2008. The future SST (futSST) and SIC (futSIC) were obtained from an ensemble of 31 RCP8.5 simulations from CMIP5 model simulations, but additional constraints were adopted to reduce the large model spread and unrealistically diffuse ice edge. More detailed information on the forcing data is provided in Appendix A of Smith et al. (2018).

Eight experimental groups were constructed representing the different combinations of the SST and SIC forcing and can be identified according to their *experiment_id* label (Table 1). The No.1.1 experimental group pdSST-pdSIC is regarded as the reference run, which was forced by the present-day SST and present-day SIC. The No.1.2 experimental group piSST-piSIC was forced by the pre-industrial SST and SIC. The difference between No.1.1 and No.1.2 can be used to identify the total effect of historical SST and SIC change on the climate. The No.1.3 experimental group piSST-pdSIC was forced by the pre-industrial SST and present-day SIC. The difference between No.1.1 and No.1.3 can be used to understand the effects of historical changes in SST on the climate. The No.1.4 experimental group futSST-pdSIC was forced by the future SST and present-day SIC. The difference between No.1.1 and No.1.4 estimates the possible climatic response to future changes in SST. The No.1.5 experimental group pdSST-piArcSIC was forced by the present-day SST and pre-industrial Arctic SIC. The difference between No.1.1 and No.1.5 indicates the possible climatic response to historical changes in Arctic SIC. The No.1.6 experimental group pdSST-futArcSIC was forced by the present-day SST and future Arctic SIC. The difference between No.1.1 and No.1.6 estimates the possible influence of future Arctic SIC changes on the climate. The No.1.7 experimental group pdSST-piAntSIC and the No.1.8 experimental group pdSST-futAntSIC are similar to the No.1.5 and 1.6 groups, respectively, but were forced by the changes of the Antarctic SIC for the pre-industrial and future conditions,

respectively.

The technological roadmap for the CAS FGOALS-f3-L large-ensemble simulations is shown in Fig. 1. Following the requirement of the PAMIP design (Table 1 in Smith et al., 2018), the radiative forcings in the atmosphere-only time-slice experiments are all prescribed as their values in 2000 (Table 1), including the greenhouse gases, solar irradiance, ozone, and aerosols in CAS FGOALS-f3-L. To provide an equilibrium state for the atmosphere and land model and the initial field for the large-ensemble simulation, we set up a control run for the spin-up process. The control run is an AMIP simulation with all the same prescribed external forcings as in pdSST-pdSIC. This experiment runs for 1st January 1990 to 1st April 2000 and provides 100 restart files every 6 hours from 7th March to 1st April 2000 for the initial field of the large-ensemble simulation as output. A total of eight groups of large-ensemble simulations are carried out, as shown in Table 1, from No.1.1 to No.1.8. Each group contains 100 simulations with a variant label of r1i1p1f1 to r100i1p1f1. For all the experiments, the initial fields are the same if the realization indexes are identical. Each member integrates from 1st April 2000 to 30th June 2001 for 14 months. The analysis for the equilibrium state could be adopted from 1st June 2000. In case the potential users are interested in the spin-up process of the CAS FGOALS-f3-L model results, we submitted and published all the integration periods on the ESG node of IAP.

The imposed external forcings in CAS FGOALS-f3-L for the present day, pre-industrial period and future are examined in this paragraph, and the calculation of the changes in SST and SIC forcing between the present day and the pre-industrial period and between the future and the present day is also documented to understand the model responses. Fig. 2a shows the annual mean spatial pattern of pdSST prescribed in the experiments of pdSST-pdSIC, pdSST-piArcSIC, pdSST-futArcSIC, pdSST-piAntSIC and pdSST-futAntSIC. As the SST forcing was obtained from the 1979-2008 mean of HadISST, the large-scale pattern of pdSST mainly shows increased temperatures in the tropics (e.g., the 28 °C isotherm mainly encloses the mid-eastern Indian Ocean and tropical western Pacific) and colder temperatures at high latitudes, with a uniform trend of -1.8 °C over the sea-ice regions. The global mean pdSST is approximately 18.19 °C. The spatial pattern of piSST is similar to that of pdSST. We show the difference between pdSST and piSST in Fig. 2b. The

difference shows an overall warming pattern, with a global mean value of 0.78 °C. The warming reaches 1.2 °C over the north Pacific and north Atlantic and exceeds 1.8 °C over the Barents Sea. The difference between the future and present SST is shown in Fig. 2c. The global mean warming is approximately 1.06 °C, which is higher than the difference between the present day and the pre-industrial period (Fig. 2b). This warming is strongest in the Northern Hemisphere, especially close to the Bering Sea, Barents Sea, and northern Atlantic.

The global mean annual cycle of the three kinds of SST forcing is shown in Fig. 3. All the SST forcings show semiannual variation, with maxima in March and August and minima in Jun and November associated with the seasonal variations in SST. The future SST is almost 1.8 °C warmer while the present day SST is 0.8 °C warmer than the pre-industrial SST in all months.

The annual mean SIC forcings for both the Arctic and Antarctic are shown in Fig. 4. For the present-day SIC (Fig. 4a), the Arctic SIC mainly covers the whole Arctic Ocean, with the ice extent covering part of the northern Pacific and northern Atlantic. The present-day Antarctic SIC (Fig. 4d) exhibits a zonally symmetric pattern with an ice extent close to 60°S. The differences between the present-day SIC and pre-industrial SIC for the Arctic and Antarctic are shown in Fig. 4b and Fig. 4e, respectively. The decrease in SIC for the Arctic mainly occurs in the latitudinal band between 50°N and 75°N. The SIC decreased by more than 30% in the Norwegian Sea and Greenland Sea. For the Antarctic, the difference between the present-day and the pre-industrial SIC is smaller overall than that in the Arctic. The decrease in SIC is approximately 5% to 10% and mainly occurs over the edge of the Antarctic mainland and at high latitudes in the South Atlantic Ocean. For the future changes in SIC, the difference between the future and present-day annual mean Arctic SIC (Fig. 4c) covers the whole Arctic Ocean, with two local minima over the Norwegian Sea and Beaufort Sea. For the Antarctic region, the decrease in SIC is approximately 10% to 15% within the latitudinal band of 60°S to 80°S and more than 20% over the Amundsen Sea. Overall, the decreases in SIC for both the Arctic and Antarctic are greater for future changes than for the present-day changes.

To quantify the changes in SIC forcing, we calculated the SIC area for each month for both the Arctic and Antarctic, and the results are presented in Table 2. The present-day SIC area shows a clear annual cycle with a maximum of 13.4×10^6 km^2 in

March and a minimum of 5.3×10^6 km^2 in September. The differences in Arctic SIC between the present day and pre-industrial period are approximately -1.4 to -1.8×10^6 km^2 for all the months. However, for the future changes in SIC, the difference between future and present-day SIC reaches -4×10^6 km^2 during the boreal summer months, which is twice the value of the present-day changes. For the Antarctic, the present-day SIC area also shows an annual cycle, but with a minimum of 2.7×10^6 km^2 in February and a maximum of 16.6×10^6 km^2 in September. The differences between the present day and pre-industrial period are approximately -1×10^6 km^2 from January to May and -1.4×10^6 km^2 from June to December. The differences between the future and present-day SIC areas are almost twice as large from April to December, ranging between -1.9×10^6 km^2 and -2.7×10^6 km^2.

3. Basic model responses to SST and SIC forcings

The basic model responses of the eight large-ensemble simulations are addressed in this section. We focus on the responses of SAT and precipitation for both the present-day changes from pre-industrial forcings and future changes from present-day forcings. The SAT and precipitation responses to present-day changes in global SST and SIC are investigated by pdSST-pdSIC minus piSST-piSIC (No.1.1-1.2). The climate responses to present-day changes in global SST alone are investigated by pdSST-pdSIC minus piSST-pdSIC (No.1.1-1.3). The climate responses to present-day changes in Arctic SIC alone are investigated by pdSST-pdSIC minus pdSST-piArcSIC (No.1.1-1.5). The climate responses to present-day changes in Antarctic SIC alone are investigated by pdSST-pdSIC minus pdSST-piAntSIC (No.1.1-1.7). For future climate changes, the model responses to future changes in global SST alone are investigated by futSST-pdSIC minus pdSST-pdSIC (No.1.4-1.1). The model responses to future changes in Arctic SIC alone are investigated by pdSST-futArcSIC minus pdSST-pdSIC (No.1.6-1.1). The model responses to future changes in Antarctic SIC alone are investigated by pdSST-futAntSIC minus pdSST-pdSIC (No.1.8-1.1).

3.1 SAT and precipitation responses to present-day forcings

Precipitation and SAT are the two most important elements for understanding global climate change, and identifying the changes in these variables is necessary to obtain quantitative knowledge of the climate model response to external forcing and

model sensitivity. To identify the basic model response of CAS FGOALS-f3-L to the present-day forcing of global SST and SIC and to understand the large-ensemble simulation spread, we first show the global mean daily evolution of the SAT over land and oceans and global precipitation of pdSST-pdSIC (No.1.1) in Fig. 5. The ensemble mean (red line) global land SAT (Fig. 5a) shows a clear annual cycle with a maximum close to 15 °C in July 2000 and a minimum close to 2 °C from December 2000 to January 2001. The large-ensemble simulation provides a range of 5 to 7 °C on the initial date of 1st April 2000. During the integration, the large-ensemble spread remains stable and becomes slightly larger from November 2000 to January 2000. As a measurement of the large-ensemble spread, the standard deviation of the global land SAT in pdSST-pdSIC is approximately 0.5 °C.

The evolution of SAT over the global ocean regions is similar overall to that of the land SAT, with a clear annual cycle (Fig. 5b) from April 2000 to June 2001. However, the variation in SAT over the ocean regions ranges from 15.7 to 16.8 °C, which is much smaller than the land SAT range. The standard deviation of the ocean SAT is approximately 0.1 °C, which suggests that the model response for ocean regions is weaker than that over land, partly because the SST is prescribed in the model. The daily evolution of the global mean precipitation is shown in Fig. 5c. The ensemble mean precipitation time series shows a semiannual cycle that is similar to that of the SST forcing in Fig. 3. This is because tropical precipitation plays a dominant role in global precipitation variation, which is mainly driven by changes in SST. The large-ensemble spread is also quite stable during the integration, and the standard deviation is approximately 0.2 mm day^{-1}.

The above analysis shows the basic performance of the CAS FGOALS-f3-L large-ensemble simulations for the present-day forcing. The model simulation is reasonable since the ensemble spread is stable during the whole integration under the fixed external forcing. To understand the relative contributions of present-day changes in SST and SIC to polar amplification, we show the ensemble mean differences in the annual mean SAT response to the four combinations in Fig. 6. The SAT responses to both the global SST and SIC changes (pdSST-pdSIC minus piSST-piSIC) are shown in Fig. 6a. The SAT anomaly shows a unified global warming pattern accompanied by polar amplification in both hemispheres. This warming pattern is similar to the observed global warming trend during the last century (Fig. TS.2 in IPCC, 2013),

which also suggests that the experimental design of the PAMIP could reasonably reproduce the observed global warming through large-ensemble simulation. In the Arctic, the SAT anomaly shows several local maxima exceeding 1.8 °C over the Barents/Kara Sea, the Okhotsk Sea, the Bering Strait, Hudson Bay, Baffin Bay and the Greenland Sea. In the Antarctic, the SAT reaches its maximum along the Antarctic mainland coast from 90 °E to 60 °W, which includes the Ross Sea, Amundsen Sea, Bellingshausen Sea, and Weddell Sea.

The SAT responses to only the global SST changes (pdSST-pdSIC minus piSST-pdSIC) show a unified global warming pattern (Fig. 6b). However, the polar amplification pattern disappeared in this pair of experiments. There are several local maxima of SAT over the northern part of the Asian mainland, the Barents Sea and northwestern North America of approximately 1.2 °C. The SAT response to the historical changes in Arctic SIC forcing (Fig. 6c, pdSST-pdSIC minus pdSST-piArcSIC) shows limited warming in the regions surrounding the Arctic Ocean. The SAT changes over other regions of the globe are very small. The SAT anomaly reaches its maximum mainly over the areas where the prescribed Arctic SIC decreases (Fig. 4b), and this pattern is also similar to the polar amplification pattern shown in Fig. 6a. Similarly, in the Antarctic, the SAT increases only in the ocean regions (Fig. 6d) where the prescribed Antarctic SIC decreases (Fig. 4e). The above results suggest that the polar amplification is dominantly controlled by the changes in global SIC, especially the Arctic SIC, because the SAT changes show an obvious meridional gradient (Fig. 6c) at high latitudes, which is similar to the combined forcing of both SST and SIC (Fig. 6a).

The response of precipitation to global warming is another topic of scientific interest in terms of the estimation of global pattern changes. The large-ensemble simulation in this study provides additional evidence for understanding the relative roles of SST and SIC forcings in changes in global precipitation. We show the spatial pattern of ensemble mean differences in annual mean precipitation between pdSST-pdSIC and piSST-piSIC in Fig. 7a, which shows that the response of precipitation is apparently different from that of SAT. Precipitation increases mainly over ocean regions, including the tropical Pacific, Southwest Pacific close to the Maritime Continent, South Indian Ocean and tropical Atlantic. Furthermore, precipitation also decreases in the South Asian monsoon regions, middle tropical

Pacific, African mainland region and low latitudes of North America.

The precipitation response to the global SST forcing alone (Fig. 7b, pdSST-pdSIC and piSST-pdSIC) shows a very similar pattern to the response to SST and SIC forcing together (Fig. 7a). The response of precipitation to the changes in Arctic SIC is shown in Fig. 7c. This pattern implies that the influence of Arctic SIC on global precipitation changes is very limited compared to the impact of SST (Fig. 7b). Precipitation increases only slightly over the tropical western Pacific close to the Maritime Continent. Similarly, the influence of Antarctic SIC on the annual mean changes in precipitation is also weak (Fig. 7d). The ensemble precipitation anomalies (pdSST-pdSIC and pdSST-piAntSIC) mainly increase on the Maritime Continent by approximately 0.4 mm day^{-1}. The above result indicates that the changes in global precipitation for the present day are dominated by the changes in the global SST relative to the changes in the global SIC.

The large-ensemble simulations provide not only a robust model response by calculating the ensemble mean but also a range of the uncertainty or the possibility of model response through the analysis of the adequate ensemble members. To quantitively estimate the uncertainty of the SAT response to SST and SIC forcings, in this study, we calculated the probability density distribution (PDF) of the SAT anomalies of 100 ensemble cases for each pair of experiments in Fig. 8. For pdSST-pdSIC minus piSST-piSIC, the global mean SAT anomaly increases to 1 °C for more than 25% of the cases. The SAT maximum is approximately 1.1 °C for about 5% of the cases, and the minimum is approximately 0.9 for about 5% of the cases.

For the cases forced by global SST changes alone (Fig. 8b, pdSST-pdSIC minus piSST-pdSIC), more than 20% simulate global mean SAT anomalies ranging from 0.88 °C to 0.92 °C. The SAT maximum is approximately 1.04 °C for only 1% of the cases, while the minimum is approximately 0.81 for 9% of the cases. Because the SAT responses to the Arctic and Antarctic SIC are quite local, we calculated the PDF of the regional mean SAT (45-90°N) anomalies for the cases of pdSST-pdSIC minus pdSST-piArcSIC and the regional mean SAT (45-90°S) anomalies for the cases of pdSST-pdSIC minus pdSST-piAntSIC in Fig. 8b and 8d, respectively. The results show that the SAT anomalies range from -0.3 °C (3% cases) to 1.0 °C (6% cases) in the middle and high latitudes in the Northern Hemisphere, with more than 20% of the cases simulating a SAT anomaly of 0.5 °C. The SAT anomalies are smaller in the

433 Southern Hemisphere middle and high latitudes (Fig. 8d). More than 15% of the cases
434 simulate a SAT anomaly of 0.15 °C. The maximum is approximately 0.3 °C for nearly
435 10% of the cases and -0.05 °C for another 5% of the cases.
436 The PDFs of the precipitation anomalies for these cases are shown in Fig. 9.
437 Because the precipitation responses mainly occur in the low latitudes, we only
438 calculated the PDF for the regional mean (45°S-45°N) precipitation anomalies. In the
439 cases of pdSST-pdSIC minus piSST-piSIC (Fig. 9a), the precipitation anomalies range
440 from 0.062 mm day^{-1} (2% of cases) to 0.108 mm day^{-1} (5% of cases), with most of the
441 cases simulating from 0.08 mm day^{-1} to 0.09 mm day^{-1}. The PDF of pdSST-pdSIC
442 minus piSST-pdSIC (Fig. 9c) is very similar to the PDF of pdSST-pdSIC minus
443 piSST-piSIC (Fig. 9a), which is also consistent with the ensemble mean results in Fig.
444 7a,b.
445 It is worth noting that the precipitation anomalies are all positive in the above
446 two pairs of experiments, which is mainly caused by the unified surface warming in
447 the low latitudes (Fig. 6a,b), but for the cases in pdSST-pdSIC minus
448 pdSST-piArcSIC (Fig. 9b) and pdSST-pdSIC minus pdSST-piAntSIC (Fig. 9d), the
449 sign of the precipitation anomalies remains uncertain. The PDF for both pairs of
450 experiments appears to be a normal-like distribution, with almost 50% of cases
451 negative and the other 50% of cases positive. Specifically, the precipitation anomalies
452 range from -0.02 mm day^{-1} to 0.02 mm day^{-1} due to the Arctic SIC forcing (Fig. 9b)
453 and range from -0.028 mm day^{-1} to 0.02 mm day^{-1} due to the Antarctic SIC forcing
454 (Fig. 9d). Furthermore, the precipitation response is approximately -0.01 mm day^{-1} for
455 nearly 20% of the cases and 0.01 mm day^{-1} for another 20% of the cases under
456 Antarctic SIC forcing, which is different from the cases under Arctic SIC forcing.
457
458 *3.2 SAT and precipitation responses to future forcings*
459 The design of future condition experiments in the PAMIP aims to assess and
460 understand the process of future climate variability and predictability. These
461 experiments are also designed for comparison with the experiments forced by
462 present-day changes to understand the atmospheric responses to different SST and
463 SIC forcings. As shown in Section 2, the future changes in SST and SIC are overall
464 larger than the present-day (relative to pre-industrial) changes. This implies that the
465 model responses to the SST and SIC will be stronger under future forcing changes

than under present-day forcing changes. We show the influence of future global SST changes on the SAT in Fig. 10a. It is clear that the SAT anomaly exhibits a global warming pattern and is warmer than the differences between pdSST-pdSIC and piSST-pdSIC (Fig. 6b). Specifically, the SAT increases 1.0 to 1.2°C in most of the region and exceeds 1.8°C in Alaska, the central Asian mainland, eastern and southern Africa, and the Antarctic mainland.

Interestingly, the Antarctic mainland is much warmer than the mid- and high-latitude oceans in the Southern Hemisphere, which is quite different from the response to present-day forcing (Fig. 6b). This result implies that SST warming could contribute to polar amplification in the Southern Hemisphere in the future. The SAT response to future changes in Arctic SIC forcing (pdSST-futArcSIC minus pdSST-pdSIC) is shown in Fig. 10b, which shows that the SAT warming mainly occurs in the Arctic region where the prescribed SIC decreases (Fig. 4c). The increase in SAT exceeds 1.8 °C over the Barents/Kara Sea, the Bering Strait, Hudson Bay, Baffin Bay and the Greenland Sea, which contributes to Arctic amplification in future projections.

For the future Antarctic SIC decrease (Fig. 10c), the SAT anomaly increases mainly along the coast of the western Antarctic mainland, and a large warming area appears over the Weddell Sea. The surface warming also corresponds with the decrease in SIC in Fig. 4f but does not show a one-to-one correspondence: the SIC decreases 20-25% over the Amundsen Sea and 5-10% over the Weddell Sea. This result implies that atmospheric dynamics play an important role in surface warming in the Antarctic.

The precipitation responses to future changes in SST and SIC are shown in Fig. 11. For the future global SST forcing changes (Fig. 11a), the precipitation mainly increases along the Intertropical Convergence Zone (ITCZ), middle latitudes in the South Pacific and high latitudes in the northern Pacific. The precipitation also shows a weak decrease in South Asia, especially on the Indo-China peninsula. This pattern is generally similar to the precipitation response to the present-day SST forcing changes (Fig. 7b), but the positive precipitation anomaly over the tropical Indian Ocean and southeastern Pacific declines in the future projection (Fig. 11a). The precipitation responses to the future Arctic SIC changes (pdSST-futArcSIC minus pdSST-pdSIC) and the future Antarctic SIC changes (pdSST-futAntSIC minus pdSST-pdSIC) are

499 shown in Fig. 11b and c, respectively. In these two pairs of experiments, the
500 precipitation responses are weak and show only a small decrease on the Maritime
501 Continent and a small increase over the middle Pacific. The above results indicate that
502 the precipitation responses to the future SST and SIC forcings are more or less similar
503 to the responses to the present-day forcings, although the magnitude of the future SST
504 and SIC changes is larger than that of the present-day changes.
505 To estimate the large-ensemble spread of the annual mean SAT and precipitation
506 response to the future changes in global SST and SIC and to compare the future
507 climate response with the present-day climate response, we show the PDF analysis for
508 all the future experiments in Fig. 12. Under the future SST forcing changes (Fig. 12a,
509 futSST-pdSIC minus pdSST-pdSIC), 30% of the cases simulate an SAT increase of
510 1.22 °C. The SAT anomaly maximum is approximately 1.38 °C for 5% of the cases,
511 and the minimum is approximately 1.12 °C for 2% of the cases. These SAT responses
512 are stronger overall than the large-ensemble simulations of the present-day responses
513 (Fig. 8c).
514 The regional SAT responses over mid-high latitudes in the Northern Hemisphere
515 (45-90°N) to the future Arctic SIC changes (Fig. 12b) are approximately 0.7 °C for
516 20% of the cases, with a maximum of 1.25 °C for 2% of the cases and 0.1 °C for 2%
517 of the cases. This PDF also supports our previous analysis of ensemble mean results
518 showing that the SAT response to future forcing is higher overall than the present-day
519 response (Fig. 8b) of approximately 0.2 °C. For the cases of pdSST-futAntSIC minus
520 pdSST-pdSIC (Fig. 12c), the SAT responses to the Antarctic SIC forcing show an
521 increase of 0.2 °C for nearly 25% of the cases, with a maximum of 0.38 °C for 1% of
522 the cases and a minimum of -0.05 °C for another 6% of the cases. This PDF is quite
523 close to the SAT present-day response (Fig. 8d), which implies that the SAT responses
524 over high latitudes in the Southern Hemisphere are not very sensitive to Antarctic SIC
525 forcing changes.
526 For the PDF of the precipitation responses to the future SST forcing changes (Fig.
527 12d), almost 24% of the cases simulate an increase in low-latitude mean precipitation
528 of 0.12 mm day^{-1}, while nearly 8% of the cases simulate 0.14 mm day^{-1} for the
529 maximum and 2% of the cases simulate 0.09 mm day^{-1} for the minimum. Compared
530 to the present-day response (Fig. 9c), the precipitation anomaly is more strongly
531 associated overall with the warmer SST in the future. The PDF for the precipitation

response to the future Arctic SIC forcing changes shows that precipitation will decrease for nearly 50% of the cases and increase for the other 50% of the cases. This distribution is quite similar to the precipitation responses to the future Antarctic SIC forcing changes (Fig. 12f), which are both close to the present-day responses in Fig. 9b and 9d. These results suggest that the influence of global SIC forcing on precipitation remains largely uncertain. The reasons and the associated physical mechanisms need further study through the diagnosis of atmospheric dynamics.

4. Discussion and Conclusions

In this study, we introduced eight groups of atmosphere-only time-slice experiments of the PAMIP carried out based on CAS FGOALS-f3-L and evaluated the basic model responses to global SST and SIC forcing for both present-day and future changes. The results indicate that Arctic amplification is caused by both an increase in global SST and a decrease in Arctic SIC. Furthermore, the decrease in the Arctic SIC is the key factor in the formation of the meridional SAT gradient in the mid-high latitudes of the Northern Hemisphere.

The relative effects of SST and SIC and their combined effect on Arctic amplification are discussed here by using the large-ensemble simulations of No.1.1 (pdSST-pdSIC), No.1.2 (piSST-piSIC), No.1.3 (piSST-pdSIC) and No.1.5 (pdSST-piArcSIC). We define the present-day changes in SAT at mid-high latitudes (45-90°N) calculated by the differences between pdSST-pdSIC and piSST-piSIC as SAT_{all} for the combined effect of global SST and Arctic SIC on Arctic amplification. The differences between pdSST-pdSIC and piSST-pdSIC are denoted by SAT_{sst} for the effect of global SST alone. The differences between pdSST-pdSIC and pdSST-piArcSIC are denoted by SAT_{Arc} for the effect of Arctic SIC alone. Moreover, the sum of SAT_{sst} and SAT_{Arc} is denoted by SAT_{sum}, which represents the linear effect of SST and SIC. The comparison of SAT_{sum} and SAT_{all} could serve as an estimate of the combined influence of SST and SIC on Arctic amplification.

We provide a scatter plot of the annual mean SAT responses by using the large-ensemble members in Fig. 13. The abscissa represents SAT_{all}, and the vertical coordinate denotes SAT_{sst} for red dots, SAT_{Arc} for black five-pointed stars, and SAT_{sum} for blue asterisks. The linear regressions of SAT_{sst}, SAT_{Arc}, and SAT_{sum} on SAT_{all} are also represented by the regression lines of the corresponding colors. The regression

coefficients are shown in the upper left corner. The results suggest that the SAT responses to the global SST alone (SAT_{sst}) could contribute to almost half of the SAT changes through the combined effects of SST and SIC (SAT_{all}), with regression coefficients of 0.49. The SAT responses to the Arctic SIC alone (SAT_{Arc}) could contribute to more than half of the SAT changes induced by the combined effects of SST and SIC (SAT_{all}), with regression coefficients of 0.63. The linear sum (SAT_{sum}) of SAT_{sst} and SAT_{Arc} is compatible with SAT_{all}, and the regression coefficient is 1.12. This result also implies that the Arctic amplification featured by the accelerated surface warming rate in the Arctic regions can be roughly estimated by the direct sum of the SAT changes from the independent SST and SIC forcing experiments. Furthermore, the combined influence of SST and SIC tends to weaken their influence on Arctic amplification.

Finally, the main conclusions of this paper are as follows. The CAS FGOALS-f3-L climate model was used to carry out the atmosphere-only time-slice experiments of the PAMIP from No.1.1 to No.1.8 and considers different combinations of the global SST, Arctic SIC and Antarctic SIC for both the present-day and future changes. The time-lag method was used for the generation of the initial fields for the large-ensemble simulations. Each group contained 100 members and was integrated from 1st April 2000 to 30th June 2001. The preliminary analysis of the SAT and precipitation responses to the present-day and future forcing suggests that Arctic amplification is dominantly controlled by changes in the Arctic SIC. The SAT responses to the Arctic SIC changes show an obvious meridional gradient over high latitudes, which is similar to the results from the combined forcing of SST and SIC. However, the changes in global precipitation for the present day are dominated by the changes in the global SST relative to the changes in SIC, partly because tropical precipitation is mainly driven by local SST forcing. The future model response is similar overall to the present-day response; in particular, the future response is stronger than the present-day response due to the larger forcing changes.

The uncertainty of the model responses was also investigated by the analysis of the large ensemble members. The global SAT response to the present-day global SST and SIC forcing shows overall positive anomalies that range from 0.9 °C (5% of cases) to 1.1 °C (5% of cases), and the SAT ranges from 1.12 °C (2% of cases) to 1.38 °C (5% of cases) for future forcing changes, while the low-latitude precipitation response

shows a range of 0.062 mm day^{-1} (2% of cases) to 0.108 mm day^{-1} (5% of cases) for present-day forcing changes and 0.09 mm day^{-1} (2% of cases) to 0.14 mm day^{-1} (8% of cases) for future forcing changes. All the above model experiments and results will contribute to PAMIP multimodel analysis and improve the understanding of polar amplification.

It is necessary to note that the conclusions made in this study still remain model dependent from the perspective of both the model physics and experimental design. The atmosphere-only experiments in the PAMIP can only diagnose the effects forced by SST and SIC alone. The roles of air-sea interactions and the interactions between the ocean and sea ice cannot be investigated with this kind of experiment. These interactions are important for the simulations of meridional atmospheric and oceanic heat transport and the associated climate feedback processes, which are also important for the understanding of polar amplification and the prediction of future climate change. Therefore, similar experiments using an air-sea couple model will be performed in the future for comparison with the atmospheric model results.

Multimodel analysis is another approach used to reduce the uncertainties arising from individual model results. Multimodel ensemble analysis of all the PAMIP model outputs is also encouraged to be carried out for more robust conclusions in understanding the causes and effects of polar amplification. Finally, this paper presents the SAT and precipitation responses to SST and SIC forcing, but the associated physical processes are not fully discussed. In particular, how the Arctic and Antarctic SIC influence low-latitude weather and climate change is the next topic we would like to address in future studies.

Data Availability Statement

The datasets used in this study is available at https://esgf-node.llnl.gov/projects/cmip6/. The DOIs for each *experiment_id* are listed in Table 1.

Acknowledgments

The research presented in this paper was jointly funded by the Strategic Priority Research Program of the Chinese Academy of Sciences (grant No. XDA19070404,

XDB40030204, and XDB40030205) and the National Natural Science Foundation of China (Grant No. 91937302 and 91837101).

REFERENCES

Abbot, D. S., & Tziperman, E. (2008). A high-latitude convective cloud feedback and equable climates. *Quarterly Journal of the Royal Meteorological Society: A journal of the atmospheric sciences, applied meteorology and physical oceanography*, *134*(630), 165-185. https://doi.org/10.1002/qj.211.

Bao, Q., Lin, P., Zhou, T., Liu, Y., Yu, Y., Wu, G., et al. (2013). The flexible global ocean-atmosphere-land system model, spectral version 2: FGOALS-s2. *Advances in Atmospheric Sciences*, *30*(3), 561-576. https://doi.org/10.1007/s00376-012-2113-9.

Bao, Q., Wu, X., Li, J., Wang, L., He, B., Wang, X., et al. (2018). Outlook for El Niño and the Indian Ocean Dipole in autumn-winter 2018–2019. *Chinese Science Bulletin*, *64*(1), 73-78. https://doi.org/10.1360/N972018-00913.

Bao, Q., & Li, J. (2020). Recent progress in climate modeling of precipitation over the Tibetan Plateau. *National Science Review*, nwaa006. https://doi.org/10.1093/nsr/nwaa006.

Barnes, E. A., & Screen, J. A. (2015). The impact of Arctic warming on the midlatitude jet-stream: Can it? Has it? Will it?. *Wiley Interdisciplinary Reviews: Climate Change*, *6*(3), 277-286. https://doi.org/10.1002/wcc.337.

Bintanja, R., Van der Linden, E. C., & Hazeleger, W. (2012). Boundary layer stability and Arctic climate change: A feedback study using EC-Earth. *Climate dynamics*, *39*(11), 2659-2673. https://doi.org/10.1007/s00382-011-1272-1.

Bretherton, C. S., & Park, S. (2009). A new moist turbulence parameterization in the Community Atmosphere Model. *Journal of Climate*, *22*(12), 3422-3448. https://doi.org/10.1175/2008jcli2556.1.

Cassano, E. N., Cassano, J. J., Higgins, M. E., & Serreze, M. C. (2014). Atmospheric impacts of an Arctic sea ice minimum as seen in the Community Atmosphere Model. *International Journal of Climatology*, *34*(3), 766-779.

https://doi.org/10.1002/joc.3723.

Clough, S. A., Shephard, M. W., Mlawer, E. J., Delamere, J. S., Iacono, M. J., Cady-Pereira, K., et al. (2005). Atmospheric radiative transfer modeling: a summary of the AER codes. *Journal of Quantitative Spectroscopy and Radiative Transfer*, *91*(2), 233-244. https://doi.org/10.1016/j.jqsrt.2004.05.058.

Cohen, J., Screen, J. A., Furtado, J. C., Barlow, M., Whittleston, D., Coumou, D., et al. (2014). Recent Arctic amplification and extreme mid-latitude weather. *Nature geoscience*, *7*(9), 627-637. https://doi.org/10.1038/ngeo2234.

Cohen, J., Jones, J., Furtado, J. C., & Tziperman, E. (2013). Warm Arctic, cold continents: A common pattern related to Arctic sea ice melt, snow advance, and extreme winter weather. *Oceanography*, *26*(4), 150-160. https://www.jstor.org/stable/24862104.

Cowtan, K., & Way, R. G. (2014). Coverage bias in the HadCRUT4 temperature series and its impact on recent temperature trends. *Quarterly Journal of the Royal Meteorological Society*, *140*(683), 1935-1944. https://doi.org/10.1002/qj.2297.

Curry, J. A., Schramm, J. L., & Ebert, E. E. (1995). Sea ice-albedo climate feedback mechanism. *Journal of Climate*, *8*(2), 240-247. https://doi.org/10.1175/1520-0442(1995)008<0240:SIACFM>2.0.CO;2.

Dai, A., Luo, D., Song, M., & Liu, J. (2019). Arctic amplification is caused by sea-ice loss under increasing CO2. *Nature communications*, *10*(1), 1-13. https://doi.org/10.1038/s41467-018-07954-9.

Eyring, V., Bony, S., Meehl, G. A., Senior, C. A., Stevens, B., Stouffer, R. J., & Taylor, K. E. (2016). Overview of the Coupled Model Intercomparison Project Phase 6 (CMIP6) experimental design and organization. *Geoscientific Model Development*, *9*(5), 1937-1958. https://doi.org/10.5194/gmd-9-1937-2016.

Gao, K., Duan, A., Chen, D., & Wu, G. (2019). Surface energy budget diagnosis reveals possible mechanism for the different warming rate among Earth's three poles in recent decades. *Science Bulletin*, *64*(16), 1140-1143. https://doi.org/10.1016/j.scib.2019.06.023.

Goosse, H., Kay, J. E., Armour, K. C., Bodas-Salcedo, A., Chepfer, H., Docquier, D., et al. (2018). Quantifying climate feedbacks in polar regions. *Nature communications*, *9*(1), 1-13. https://doi.org/10.1038/s41467-018-04173-0.

696 Gramling, C. (2015). Arctic impact. *Science* 347, 818-821.
697 https://doi.org/10.1126/science.347.6224.818.
698 Graversen, R. G., & Wang, M. (2009). Polar amplification in a coupled climate model
699 with locked albedo. *Climate Dynamics*, *33*(5), 629-643.
700 https://doi.org/10.1007/s00382-009-0535-6.
701 Guo, Y., Yu, Y., Lin, P., Liu, H., He, B., Bao, Q., et al. (2020). Overview of the CMIP6
702 Historical Experiment Datasets with the Climate System Model CAS
703 FGOALS-f3-L. *Advances in Atmospheric Sciences*, 1-10.
704 https://doi.org/10.1007/s00376-020-2004-4.
705 Hall, A. (2004). The role of surface albedo feedback in climate. *Journal of Climate*,
706 *17*(7), 1550-1568.
707 https://doi.org/10.1175/1520-0442(2004)017<1550:TROSAF>2.0.CO;2
708 Harris, L. M., & Lin, S. J. (2014). Global-to-regional nested grid climate simulations
709 in the GFDL high resolution atmospheric model. *Journal of Climate*, *27*(13),
710 4890-4910. https://doi.org/10.1175/JCLI-D-13-00596.1.
711 He, B., Yu, Y., Bao, Q., Lin, P., Liu, H., Li, J., et al. (2020). CAS FGOALS-f3-L
712 model dataset descriptions for CMIP6 DECK experiments. *Atmospheric and*
713 *Oceanic Science Letters*, 1-7. https://doi.org/10.1080/16742834.2020.1778419.
714 He, B., Bao, Q., Wang, X., Zhou, L., Wu, X., Liu, Y., et al. (2019). CAS
715 FGOALS-f3-L model datasets for CMIP6 historical atmospheric model
716 Intercomparison project simulation. *Advances in Atmospheric Sciences*, *36*(8),
717 771-778. https://doi.org/10.1007/s00376-019-9027-8.
718 Holland, M. M., & Bitz, C. M. (2003). Polar amplification of climate change in
719 coupled models. *Climate Dynamics*, *21*(3-4), 221-232.
720 https://doi.org/10.1007/s00382-003-0332-6.
721 Khodri, M., Leclainche, Y., Ramstein, G., Braconnot, P., Marti, O., & Cortijo, E.
722 (2001). Simulating the amplification of orbital forcing by ocean feedbacks in the
723 last glaciation. *Nature*, *410*(6828), 570-574. https://doi.org/10.1038/35069044.
724 Li, J., Bao, Q., Liu, Y., Wu, G., Wang, L., He, B., et al. (2019). Evaluation of FAMIL2
725 in simulating the climatology and seasonal-to-interannual variability of tropical
726 cyclone characteristics. *Journal of Advances in Modeling Earth Systems*, *11*,
727 1117–1136. https://doi.org/ 10.1029/2018MS001506
728 Lin, S. J. (2004). A “vertically Lagrangian” finite-volume dynamical core for global

models. *Monthly Weather Review*, *132*(10), 2293-2307. https://doi.org/10.1175/1520-0493(2004)132<2293:AVLFDC>2.0.CO;2.

Lin, Y. L., Farley, R. D., & Orville, H. D. (1983). Bulk parameterization of the snow field in a cloud model. *Journal of climate and applied meteorology*, *22*(6), 1065-1092. https://doi.org/10.1175/1520-0450(1983)022<1065:BPOTSF>2.0.CO;2.

Lu, J., & Cai, M. (2009). Seasonality of polar surface warming amplification in climate simulations. *Geophysical Research Letters*, *36*(16). https://doi.org/10.1029/2009GL040133.

Magnusdottir, G., Deser, C., & Saravanan, R. (2004). The effects of North Atlantic SST and sea ice anomalies on the winter circulation in CCM3. Part I: Main features and storm track characteristics of the response. *Journal of Climate*, *17*(5), 857-876. https://doi.org/10.1175/1520-0442(2004)017<0857:TEONAS>2.0.CO;2.

Manabe, S., & Wetherald, R. T. (1980). On the distribution of climate change resulting from an increase in CO2 content of the atmosphere. *Journal of the Atmospheric Sciences*, *37*(1), 99-118. https://doi.org/10.1175/1520-0469(1980)037<0099:OTDOCC>2.0.CO;2.

Manabe, S., & Wetherald, R. T. (1975). The effects of doubling the CO2 concentration on the climate of a general circulation model. *Journal of the Atmospheric Sciences*, *32*(1), 3-15. https://doi.org/10.1175/1520-0469(1975)032<0003:TEODTC>2.0.CO;2.

Manabe, S., & Stouffer, R. J. (1994). Multiple-century response of a coupled ocean-atmosphere model to an increase of atmospheric carbon dioxide. *Journal of climate*, *7*(1), 5-23. https://doi.org/10.1175/1520-0442(1994)007<0005:MCROAC>2.0.CO;2.

Mori, M., Watanabe, M., Shiogama, H., Inoue, J., & Kimoto, M. (2014). Robust Arctic sea-ice influence on the frequent Eurasian cold winters in past decades. *Nature Geoscience*, *7*(12), 869-873. https://doi.org/10.1038/ngeo2277.

Overland, J., Francis, J. A., Hall, R., Hanna, E., Kim, S. J., & Vihma, T. (2015). The melting Arctic and midlatitude weather patterns: Are they connected?. *Journal of Climate*, *28*(20), 7917-7932. https://doi.org/10.1175/JCLI-D-14-00822.1.

Overland, J. E., Wood, K. R., & Wang, M. (2011). Warm Arctic—cold continents:

762 climate impacts of the newly open Arctic Sea. *Polar Research*, *30*(1), 15787.
763 https://doi.org/10.3402/polar.v30i0.15787.
764 Palmer, T. N., Shutts, G. J., & Swinbank, R. (1986). Alleviation of a systematic
765 westerly bias in general circulation and numerical weather prediction models
766 through an orographic gravity wave drag parametrization. *Quarterly Journal of*
767 *the Royal Meteorological Society*, *112*(474), 1001-1039.
768 https://doi.org/10.1002/qj.49711247406.
769 Pithan, F., & Mauritsen, T. (2014). Arctic amplification dominated by temperature
770 feedbacks in contemporary climate models. *Nature Geoscience*, *7*(3), 181-184.
771 https://doi.org/10.1038/ngeo2071.
772 Putman, W. M., & Lin, S. J. (2007). Finite-volume transport on various cubed-sphere
773 grids. *Journal of Computational Physics*, *227*(1), 55-78.
774 https://doi.org/10.1016/j.jcp.2007.07.022.
775 Screen, J. A., & Simmonds, I. (2010). The central role of diminishing sea ice in recent
776 Arctic temperature amplification. *Nature*, *464*(7293), 1334-1337.
777 https://doi.org/10.1038/nature09051.
778 Screen, J. A., Deser, C., Simmonds, I., & Tomas, R. (2014). Atmospheric impacts of
779 Arctic sea-ice loss, 1979–2009: Separating forced change from atmospheric
780 internal variability. *Climate dynamics*, *43*(1-2), 333-344.
781 https://doi.org/10.1007/s00382-013-1830-9.
782 Screen, J. A. (2017). Far-flung effects of Arctic warming. *Nature Geoscience*, *10*(4),
783 253-254. https://doi.org/10.1038/ngeo2924.
784 Screen, J. A., Deser, C., & Simmonds, I. (2012). Local and remote controls on
785 observed Arctic warming. *Geophysical Research Letters*, *39*(10).
786 https://doi.org/10.1029/2012GL051598.
787 Screen, J. A., Deser, C., Smith, D. M., Zhang, X., Blackport, R., Kushner, P. J., et al.
788 (2018). Consistency and discrepancy in the atmospheric response to Arctic
789 sea-ice loss across climate models. *Nature Geoscience*, *11*(3), 155-163.
790 https://doi.org/10.1038/s41561-018-0059-y.
791 Seierstad, I. A., & Bader, J. (2009). Impact of a projected future Arctic sea ice
792 reduction on extratropical storminess and the NAO. *Climate dynamics*, *33*(7-8),
793 937. https://doi.org/10.1007/s00382-008-0463-x.
794 Serreze, M. C., & Francis, J. A. (2006). The Arctic amplification debate. *Climatic*

change, *76*(3-4), 241-264. https://doi.org/10.1007/s10584-005-9017-y.

Serreze, M. C., Barrett, A. P., Stroeve, J. C., Kindig, D. N., & Holland, M. M. (2009). The emergence of surface-based Arctic amplification. *The Cryosphere*, *3*(1), 11. https://doi.org/10.5194/tc-3-11-2009.

Serreze, M. C., & Barry, R. G. (2011). Processes and impacts of Arctic amplification: A research synthesis. *Global and planetary change*, *77*(1-2), 85-96. https://doi.org/10.1016/j.gloplacha.2011.03.004.

Sévellec, F., Fedorov, A. V., & Liu, W. (2017). Arctic sea-ice decline weakens the Atlantic meridional overturning circulation. *Nature Climate Change*, *7*(8), 604-610. https://doi.org/10.1038/nclimate3353.

Shepherd, T. G. (2016). Effects of a warming Arctic. *Science*, *353*(6303), 989-990. https://doi.org/10.1126/science.aag2349.

Smith, D. M., Screen, J. A., Deser, C., Cohen, J., Fyfe, J. C., García-Serrano, J., et al. (2019). The Polar Amplification Model Intercomparison Project (PAMIP) contribution to CMIP6: Investigating the causes and consequences of polar amplification. *Geoscientific Model Development*, *12*(3), 1139-1164. https://doi.org/10.5194/gmd-12-1139-2019.

Spielhagen, R. F., Werner, K., Sørensen, S. A., Zamelczyk, K., Kandiano, E., Budeus, G., et al. (2011). Enhanced modern heat transfer to the Arctic by warm Atlantic water. *Science*, *331*(6016), 450-453. https://doi.org/10.1126/science.1197397.

Stocker, T. F., Qin, D., Plattner, G. K., Tignor, M., Allen, S. K., Boschung, J., et al. (2013). Climate change 2013: The physical science basis. *Contribution of working group I to the fifth assessment report of the intergovernmental panel on climate change*, *1535*.

Stuecker, M. F., Bitz, C. M., Armour, K. C., Proistosescu, C., Kang, S. M., Xie, S. P., et al. (2018). Polar amplification dominated by local forcing and feedbacks. *Nature Climate Change*, *8*(12), 1076-1081. https://doi.org/10.1038/s41558-018-033.

Taylor, P. C., Cai, M., Hu, A., Meehl, J., Washington, W., & Zhang, G. J. (2013). A decomposition of feedback contributions to polar warming amplification. *Journal of Climate*, *26*(18), 7023-7043. https://doi.org/10.1175/JCLI-D-12-00696.1.

Vavrus, S. (2004). The impact of cloud feedbacks on Arctic climate under greenhouse

forcing. *Journal of Climate*, *17*(3), 603-615. https://doi.org/10.1175/1520-0442(2004)017<0603:TIOCFO>2.0.CO;2.

Vihma, T. (2014). Effects of Arctic sea ice decline on weather and climate: A review. *Surveys in Geophysics*, *35*(5), 1175-1214. https://doi.org/10.1007/s10712-014-9284-0.

Walsh, J. E. (2014). Intensified warming of the Arctic: Causes and impacts on middle latitudes. *Global and Planetary Change*, *117*, 52-63. https://doi.org/10.1016/j.gloplacha.2014.03.003.

Wang, X., & Zhang, M. (2014). Vertical velocity in shallow convection for different plume types. *Journal of Advances in Modeling Earth Systems*, *6*(2), 478-489. https://doi.org/10.1002/2014MS000318.

Winton, M. (2006). Amplified Arctic climate change: What does surface albedo feedback have to do with it?. *Geophysical Research Letters*, *33*(3). https://doi.org/10.1029/2005GL025244.

Xie, Y., Wu, G., Liu, Y., & Huang, J. (2020). Eurasian cooling linked with Arctic warming: Insights from PV dynamics. *Journal of Climate*, *33*(7), 2627-2644. https://doi.org/10.1175/JCLI-D-19-0073.1.

Xu, K. M., & Randall, D. A. (1996). A semiempirical cloudiness parameterization for use in climate models. *Journal of the atmospheric sciences*, *53*(21), 3084-3102. https://doi.org/10.1175/1520-0469(1996)053<3084:ASCPFU>2.0.CO;2.

Zhang, P., Wu, Y., Simpson, I. R., Smith, K. L., Zhang, X., De, B., & Callaghan, P. (2018). A stratospheric pathway linking a colder Siberia to Barents-Kara Sea sea ice loss. *Science advances*, *4*(7), eaat6025. https://doi.org/10.1126/sciadv.aat6025.

Zhou, L., Bao, Q., Liu, Y., Wu, G., Wang, W. C., Wang, X., et al. (2015). Global energy and water balance: Characteristics from Finite-volume Atmospheric Model of the IAP/LASG (FAMIL 1). *Journal of Advances in Modeling Earth Systems*, *7*(1), 1-20. https://doi.org/10.1002/2014ms000349.

858 **Figures and tables**

859

860 **Table 1.** Experimental designs of the CAS FGOALS-f3-L large-ensemble simulations
861 for the PAMIP. All atmospheric radiative forcings are prescribed as their values in
862 2000.

No.	Experiment_id	Variant label	Integration period	SST & SIC forcings	DOIs
1.1	pdSST-pdSIC	r1i1p1f1 to r100i1p1f1. The realization index denotes the different initial fields, as shown in Fig. 1. The initial fields with the same realization index values are exactly the same	1st April 2000 to 30th June 2001. The first two months represent the spin-up time, as recommended in Smith et al. (2018). We submitted all the integration periods in case the users are interested in studying the spin-up process.	Present-day SST and present-day SIC	http://doi.org/10.2033/ESGF/CMIP6.11516
1.2	piSST-piSIC			Preindustrial SST and pre-industrial SIC	http://doi.org/10.2033/ESGF/CMIP6.11521
1.3	piSST-pdSIC			Preindustrial SST and present-day SIC	http://doi.org/10.2033/ESGF/CMIP6.11520
1.4	futSST-pdSIC			Future SST and present-day SIC	http://doi.org/10.2033/ESGF/CMIP6.11500
1.5	pdSST-piArcSIC			Present-day SST and pre-industrial Arctic SIC	http://doi.org/10.2033/ESGF/CMIP6.11519
1.6	pdSST-futArcSIC			Present-day SST and future Arctic SIC	http://doi.org/10.2033/ESGF/CMIP6.11512
1.7	pdSST-piAntSIC			Present-day SST and pre-industrial Antarctic SIC	http://doi.org/10.2033/ESGF/CMIP6.11518
1.8	pdSST-futAntS			Present-day SST	http://doi.org/10.2

IC	for all the experiment_id.	and future Antarctic SIC	2033/ESGF/CMIP6.11511

863

864

865

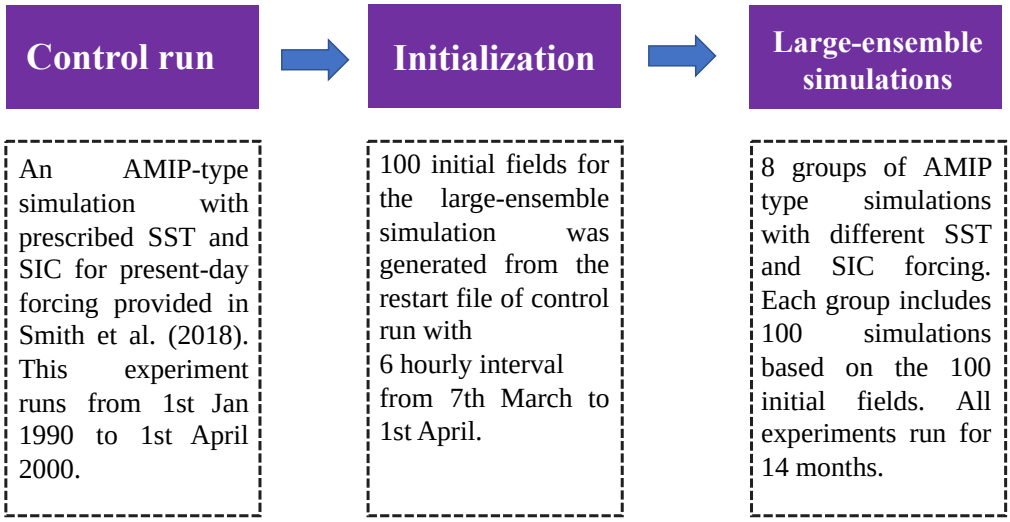

866

867 **Fig. 1.** Technological roadmap for the CAS FGOALS-f3-L large-ensemble
868 simulations. External forcings

869

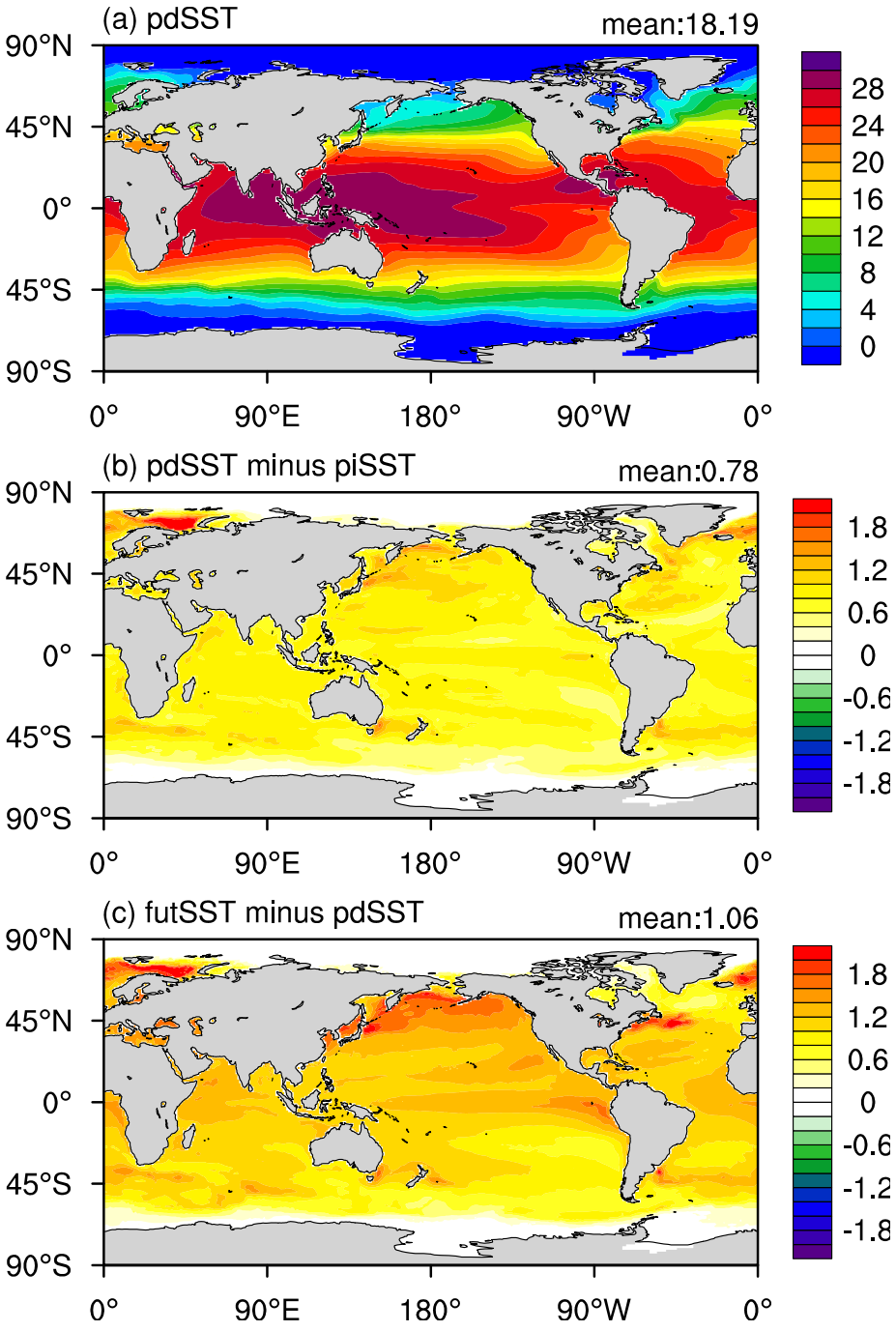

870

871

872 **Fig. 2.** Spatial distribution of annual mean SST (°C) forcings for (a) present-day SST

873 (pdSST) and (b) the difference between pdSST and pre-industrial SST (piSST) and (c)

874 between future SST (futSST) and pdSST.

875

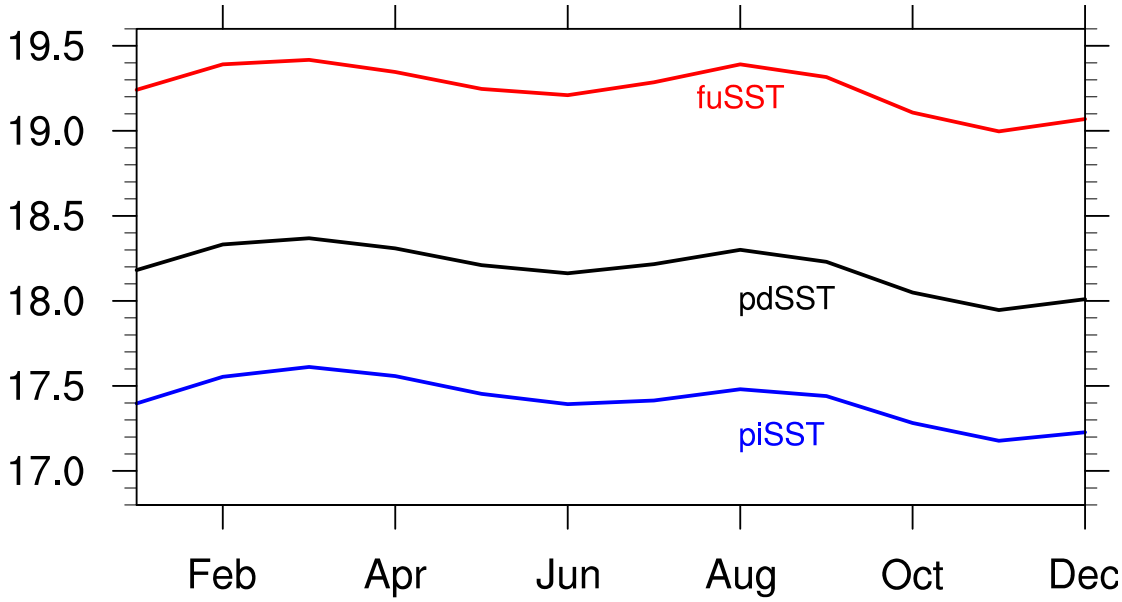

Fig. 3. Annual cycle of global mean SST forcings for present-day SST (pdSST), pre-industrial SST (piSST), and future SST (futSST).

.

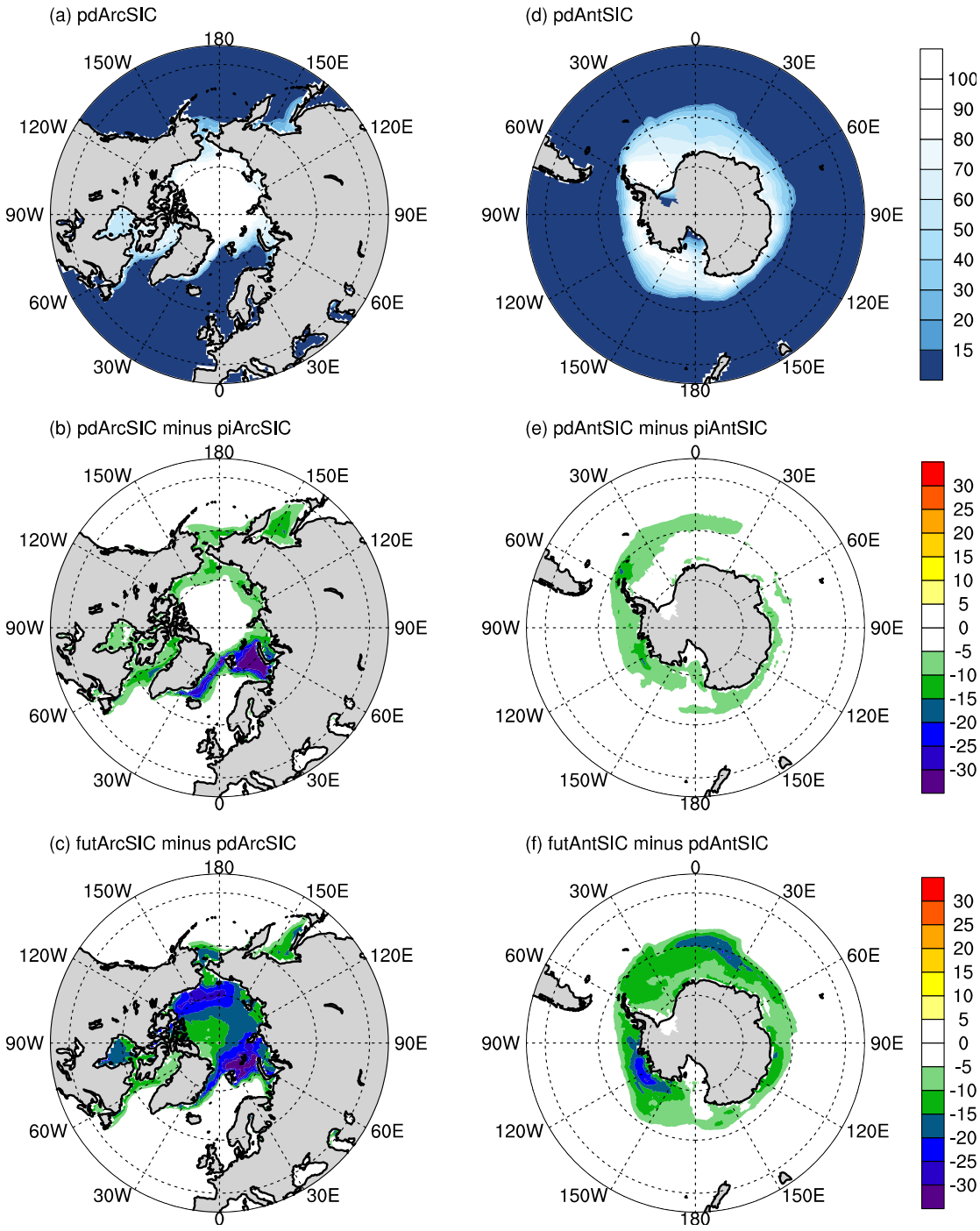

Fig. 4. Spatial distribution of annual mean SIC (%) forcings for the (a) present-day Arctic SIC (pdArcSIC), (b) difference between pdArcSIC and pre-industrial Arctic SIC (piArcSIC), (c) difference between future Arctic SIC (futArcSIC) and pdArcSIC, (d) present-day Antarctic SIC (pdAntSIC), (e) difference between pdAntSIC and pre-industrial Antarctic SIC (piAntSIC), and (f) difference between future Antarctic SIC (futAntSIC) and pdAntSIC.

Table 2. Sea ice concentration area (10^6 km^2) for pdSIC, piSIC, and futSIC

Month	Arctic					Antarctic				
	pd	pi	fut	pd-pi	fut-pd	pd	pi	fut	pd-pi	fut-pd
January	12.6	14.1	10.7	-1.5	-1.9	4.1	5.2	2.7	-1.1	-1.4
February	13.4	15	11.8	-1.5	-1.7	2.7	3.7	1.7	-0.9	-1.1
March	13.6	15.2	12	-1.6	-1.5	3.6	4.6	2.2	-1	-1.4
April	12.8	14.4	11.5	-1.6	-1.3	6.2	7.1	4.2	-0.9	-2
May	11.5	13	10.3	-1.4	-1.3	9.2	10.3	6.9	-1.1	-2.3
June	10	11.3	8.3	-1.3	-1.7	12.2	13.4	9.7	-1.3	-2.5
July	7.5	9.2	5	-1.7	-2.5	14.6	15.9	12.1	-1.4	-2.5
August	5.7	7.5	2.2	-1.8	-3.5	16	17.4	13.5	-1.4	-2.5
September	5.3	7.1	1.3	-1.8	-4	16.6	18	14	-1.4	-2.6
October	7.2	9	2.7	-1.8	-4.5	16.1	17.5	13.4	-1.4	-2.7
November	9.4	10.8	5.9	-1.4	-3.4	13.5	14.9	11	-1.4	-2.4
December	11.3	12.7	8.6	-1.5	-2.7	8.2	9.6	6.3	-1.4	-1.9

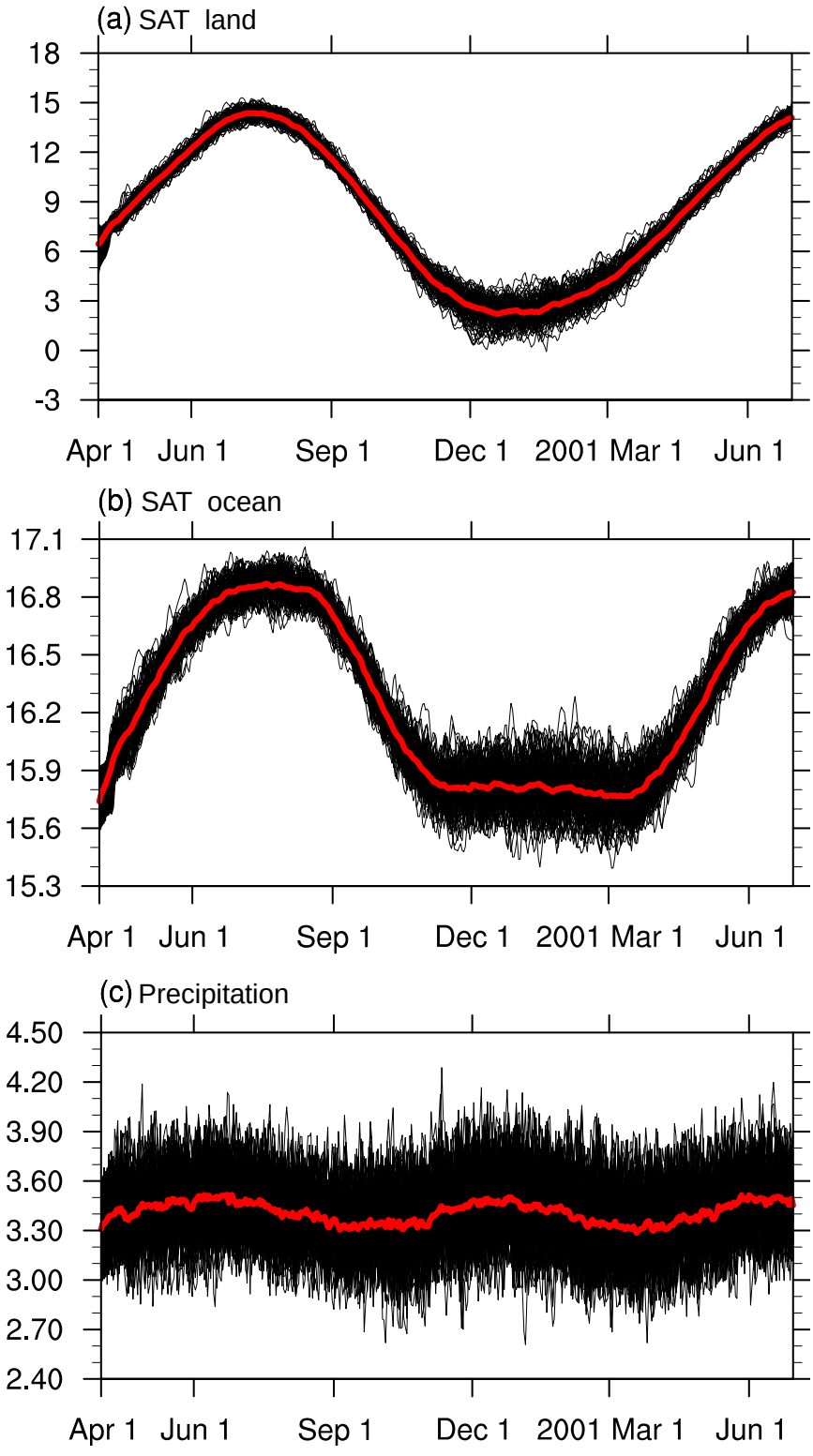

Fig. 5. Time series of global mean daily SAT (°C) for the (a) global land, (b) global ocean and (c) precipitation (mm day^{-1}) in pdSST_pdSIC. The red line denotes the ensemble mean results, and the black lines represent 100 ensemble members. The standard deviation of SAT is 0.5 °C over land and 0.1 °C over ocean. The standard deviation of global precipitation is 0.2 mm day^{-1}.

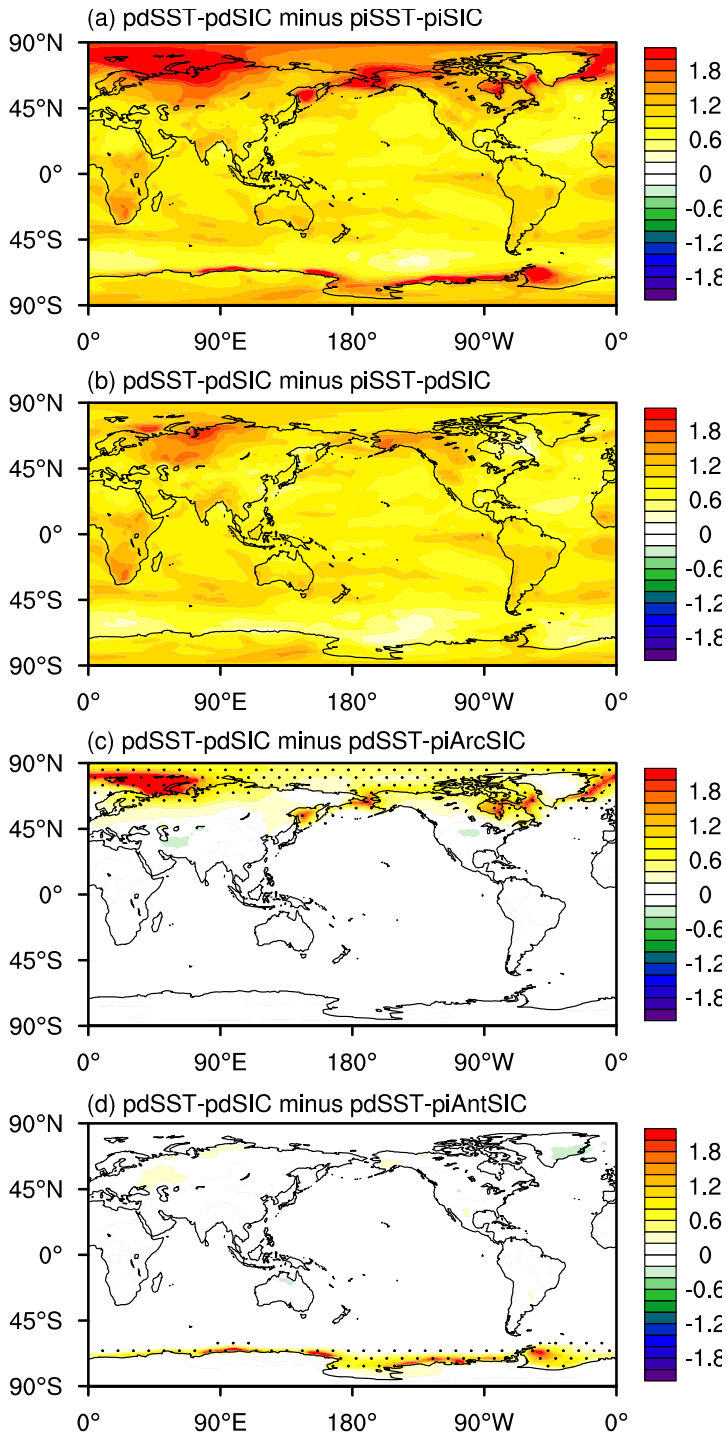

Fig. 6. Spatial pattern of ensemble mean differences in annual mean SAT (°C) response in the following experiments: (a) pdSST-pdSIC minus piSST-piSIC, (b) pdSST-pdSIC minus piSST-pdSIC, (c) pdSST-pdSIC minus pdSST-piArcSIC, and (d) pdSST-pdSIC minus pdSST-piAntSIC. All the SAT responses in (a) and (b) and the black dots in (c) and (d) are statistically significant at the 99% confidence level

914 according to Student's *t* test.

915

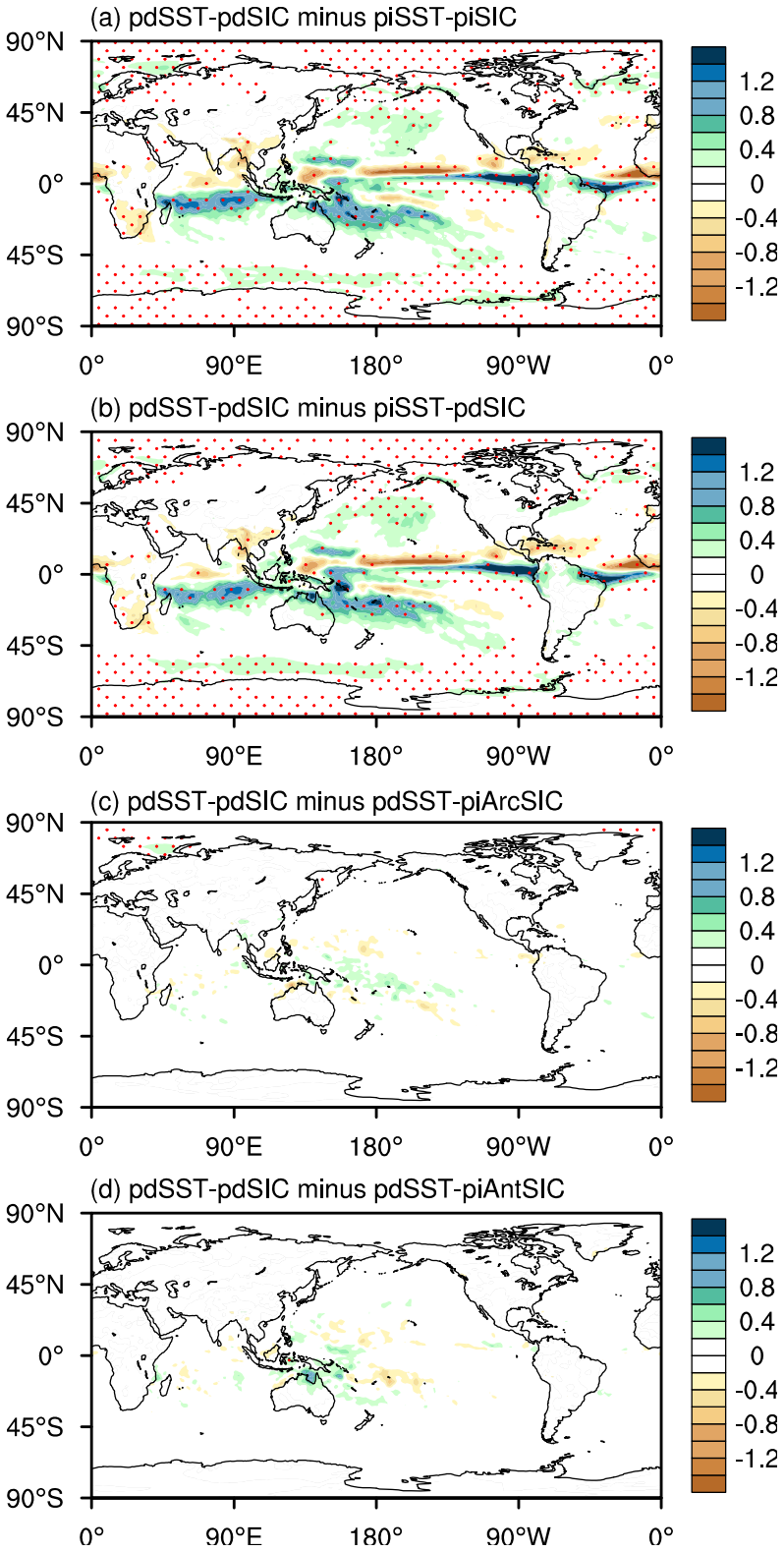

916

917 **Fig. 7.** Spatial pattern of ensemble mean differences in annual mean precipitation
918 (mm day^{-1}) response in the following experiments: (a) pdSST-pdSIC minus
919 piSST-piSIC, (b) pdSST-pdSIC minus piSST-pdSIC, (c) pdSST-pdSIC minus

pdSST-piArcSIC, and (d) pdSST-pdSIC minus pdSST-piAntSIC. The red dots denote values that are statistically significant at the 99% confidence level according to Student's *t* test.

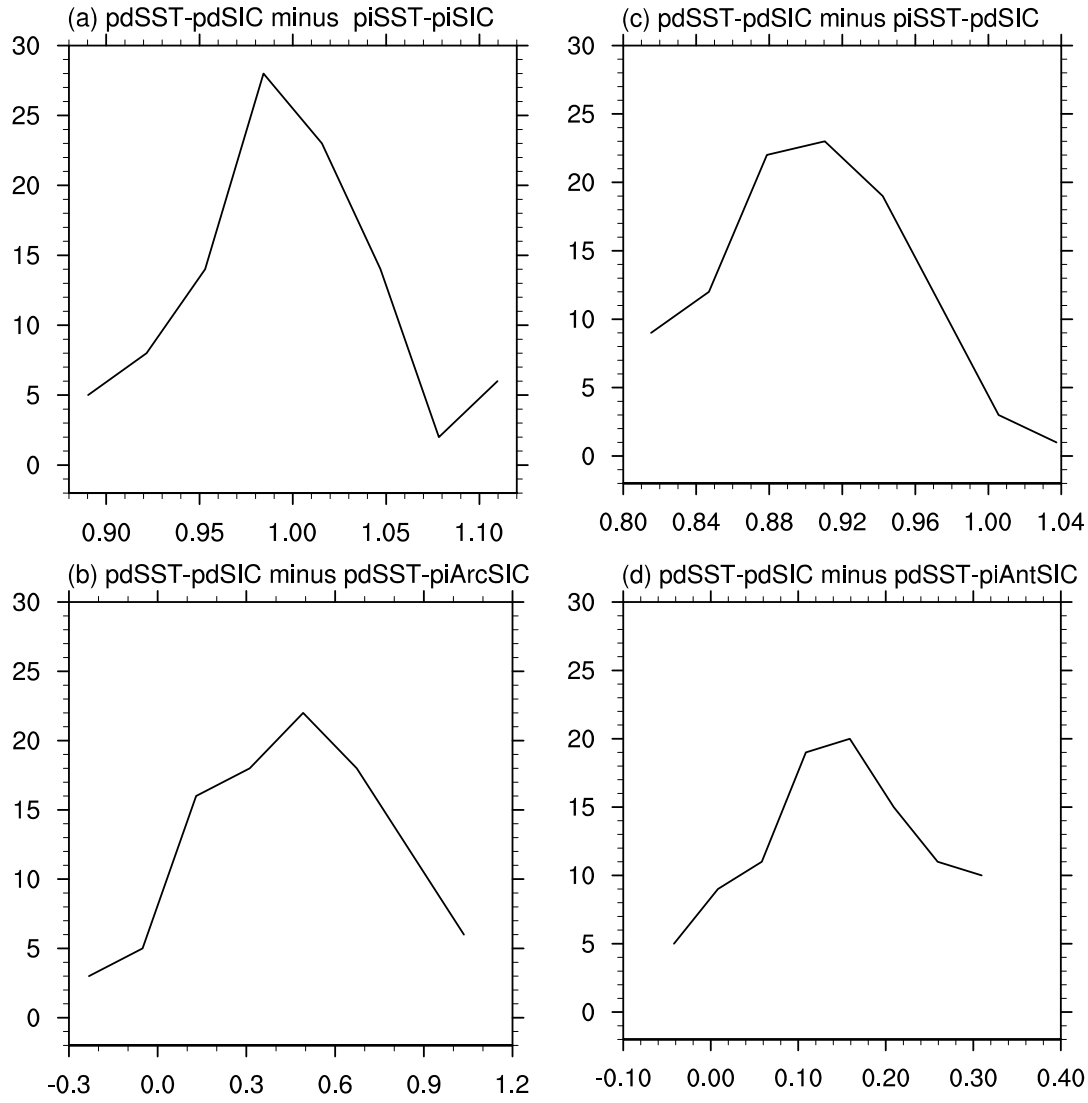

Fig. 8. Probability density distribution of (a) global mean SAT anomalies of pdSST-pdSIC minus piSST-piSIC, (c) global mean SAT anomalies of pdSST-pdSIC minus piSST-pdSIC, (b) regional mean (45-90°N) SAT anomalies of pdSST-pdSIC minus piSST-piArcSIC, and (d) regional mean (45-90°S) SAT anomalies of pdSST-pdSIC minus piSST-piAntSIC. The abscissa denotes the SAT anomalies (°C), and the vertical coordinate denotes the associated probability density distribution.

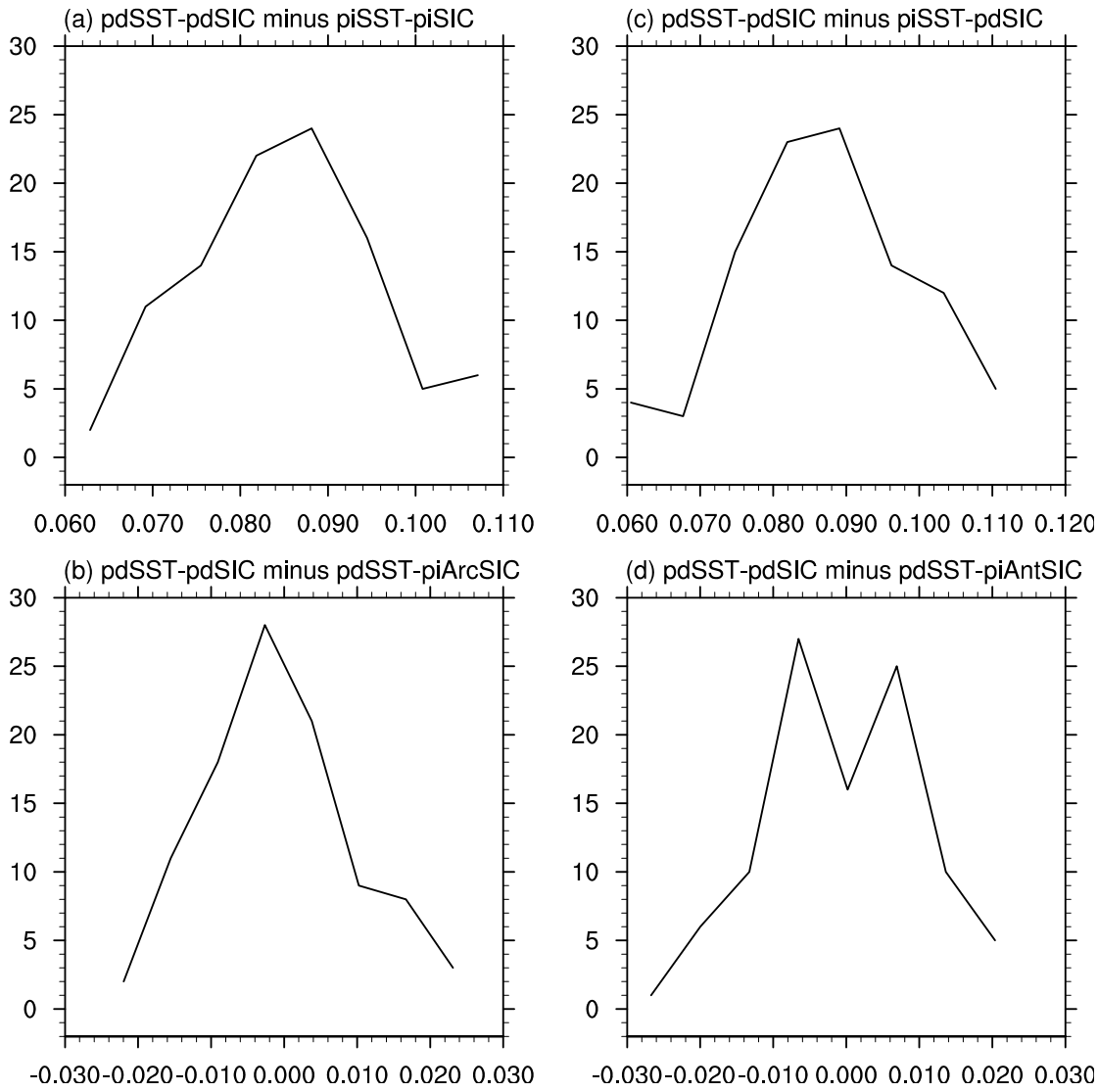

Fig. 9. Probability density distribution of regional mean (45°S-45°N) precipitation anomalies for the experiments of (a) pdSST-pdSIC minus piSST-piSIC, (c) pdSST-pdSIC minus piSST-pdSIC, (b) pdSST-pdSIC minus piSST-piArcSIC, and (d) pdSST-pdSIC minus piSST-piAntSIC. The abscissa denotes the precipitation anomalies (mm day^{-1}), and the vertical coordinate denotes the associated probability density distribution.

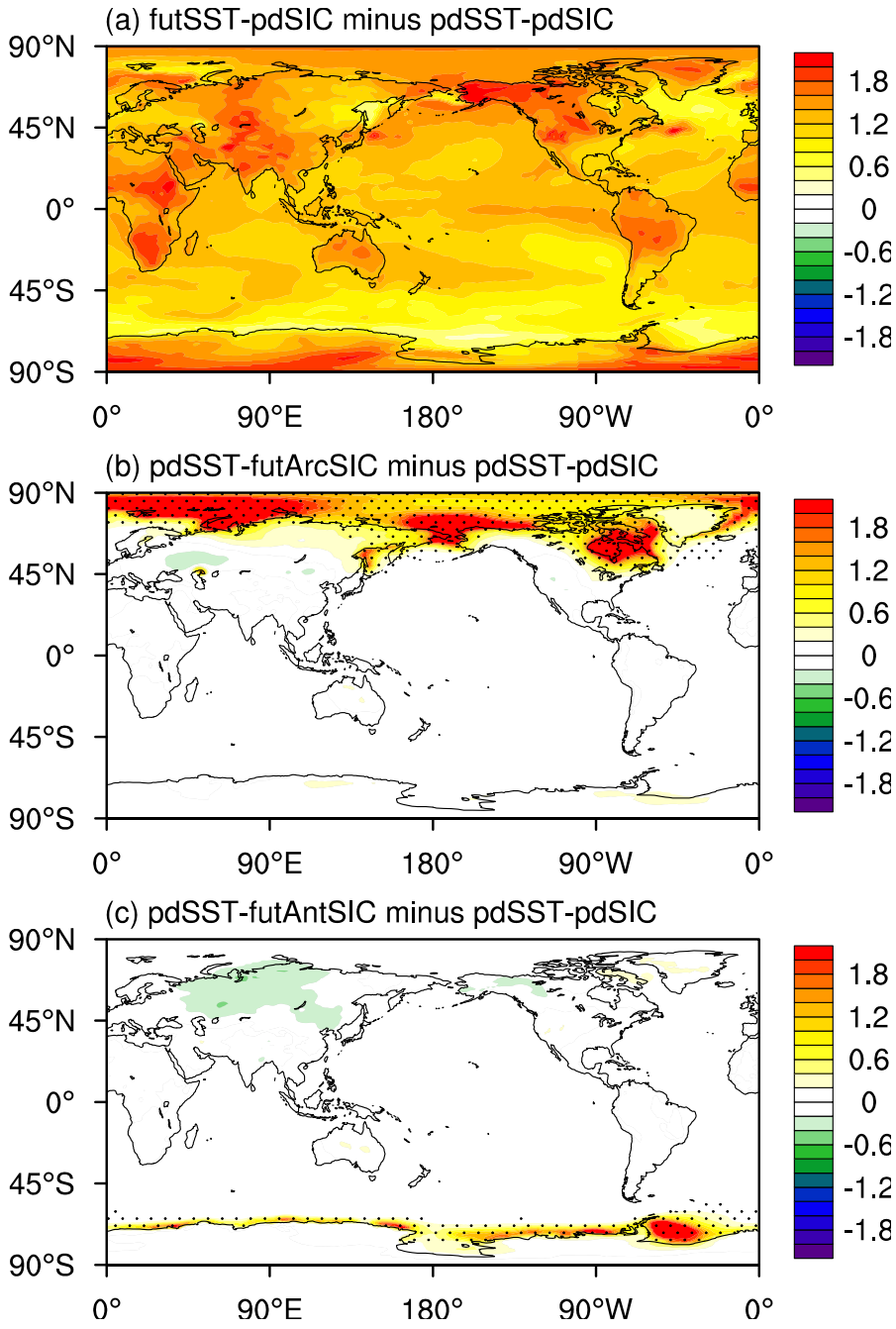

Fig. 10. Spatial pattern of ensemble mean differences in annual mean SAT (°C) response in the following experiments: (a) futSST-pdSIC minus pdSST-pdSIC, (b) pdSST-futArcSIC minus pdSST-pdSIC, and (c) pdSST-futAntSIC minus pdSST-pdSIC. All the SAT responses in (a) and the black dots in (b) and (c) are statistically significant at the 99% confidence level according to Student's *t* test.

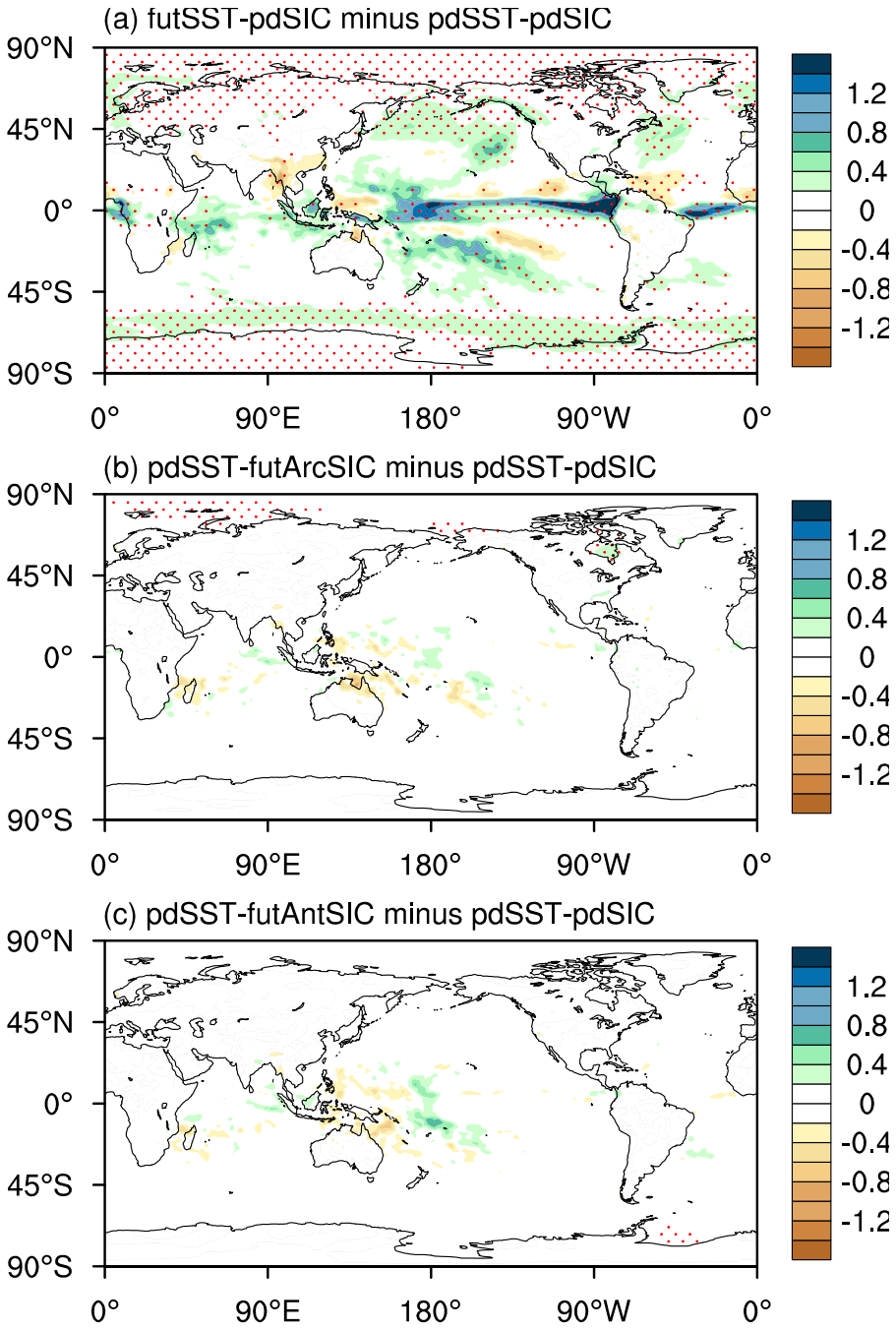

Fig. 11. Spatial pattern of ensemble mean differences in annual mean precipitation (mm day^{-1}) response in the following experiments: (a) futSST-pdSIC minus pdSST-pdSIC, (b) pdSST-futArcSIC minus pdSST-pdSIC, and (c) pdSST-futAntSIC minus pdSST-pdSIC. The red dots denote the values that are statistically significant at the 99% confidence level according to Student's *t* test.

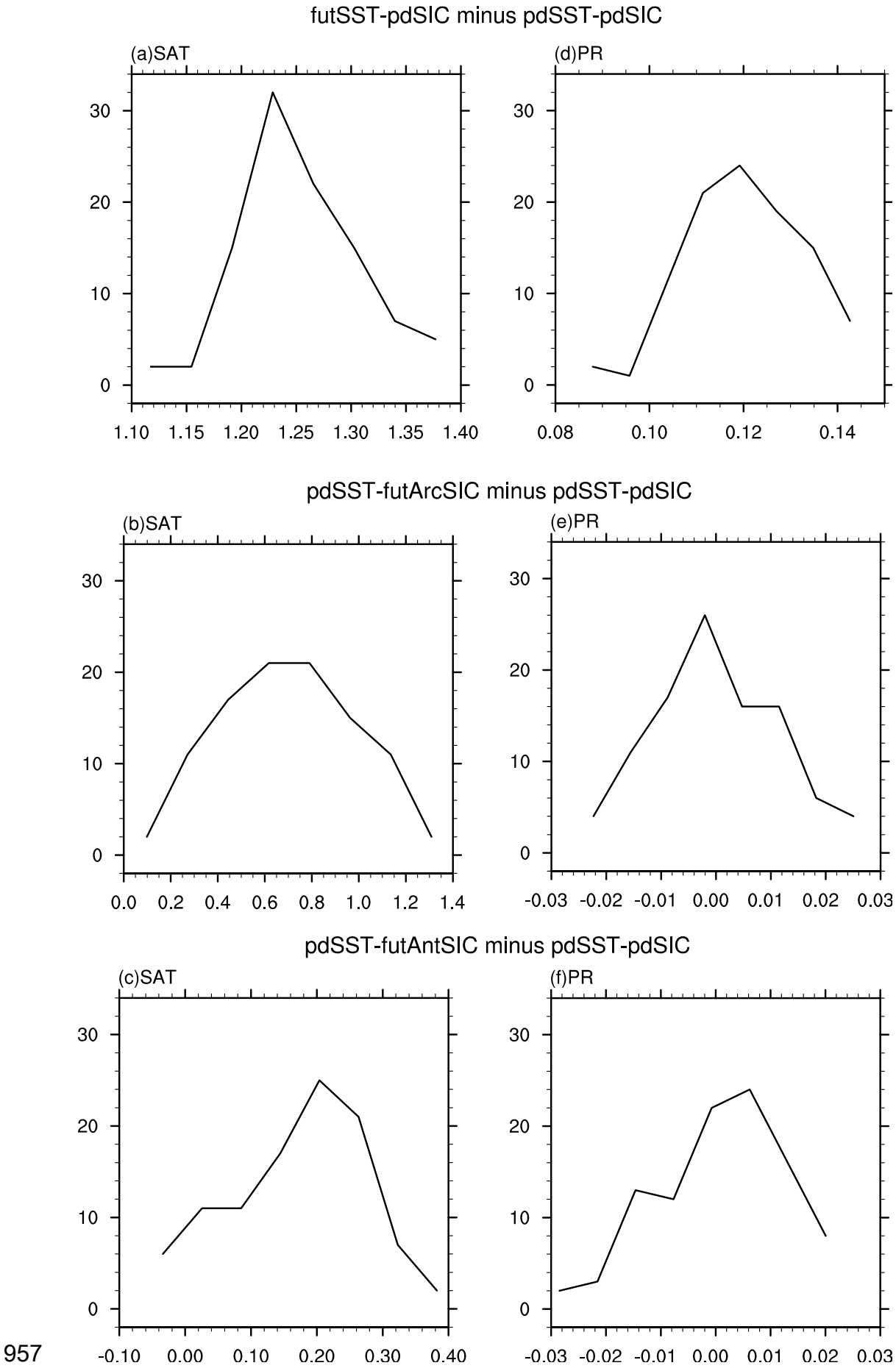
futSST-pdSIC minus pdSST-pdSIC
(a)SAT
(d)PR
pdSST-futArcSIC minus pdSST-pdSIC
(b)SAT
(e)PR
pdSST-futAntSIC minus pdSST-pdSIC
(c)SAT
(f)PR

957

Fig. 12. Probability density distribution of (a) global mean SAT anomalies of futSST-pdSIC minus pdSST-pdSIC, (b) regional mean (45-90°N) SAT anomalies of pdSST-futArcSIC minus pdSST-pdSIC, and (c) regional mean (45-90°S) SAT anomalies of pdSST-futAntSIC minus pdSST-pdSIC. The abscissa denotes the SAT anomalies (°C), and the vertical coordinate denotes the associated probability density distribution. Probability density distribution of regional mean (45°S-45°N) precipitation anomalies for the experiments of (d) futSST-pdSIC minus piSST-pdSIC, (e) pdSST-futArcSIC minus pdSST-pdSIC, and (f) pdSST-futAntSIC minus pdSST-pdSIC. The abscissa denotes the precipitation anomalies (mm day^{-1}), and the vertical coordinate denotes the associated probability density distribution.

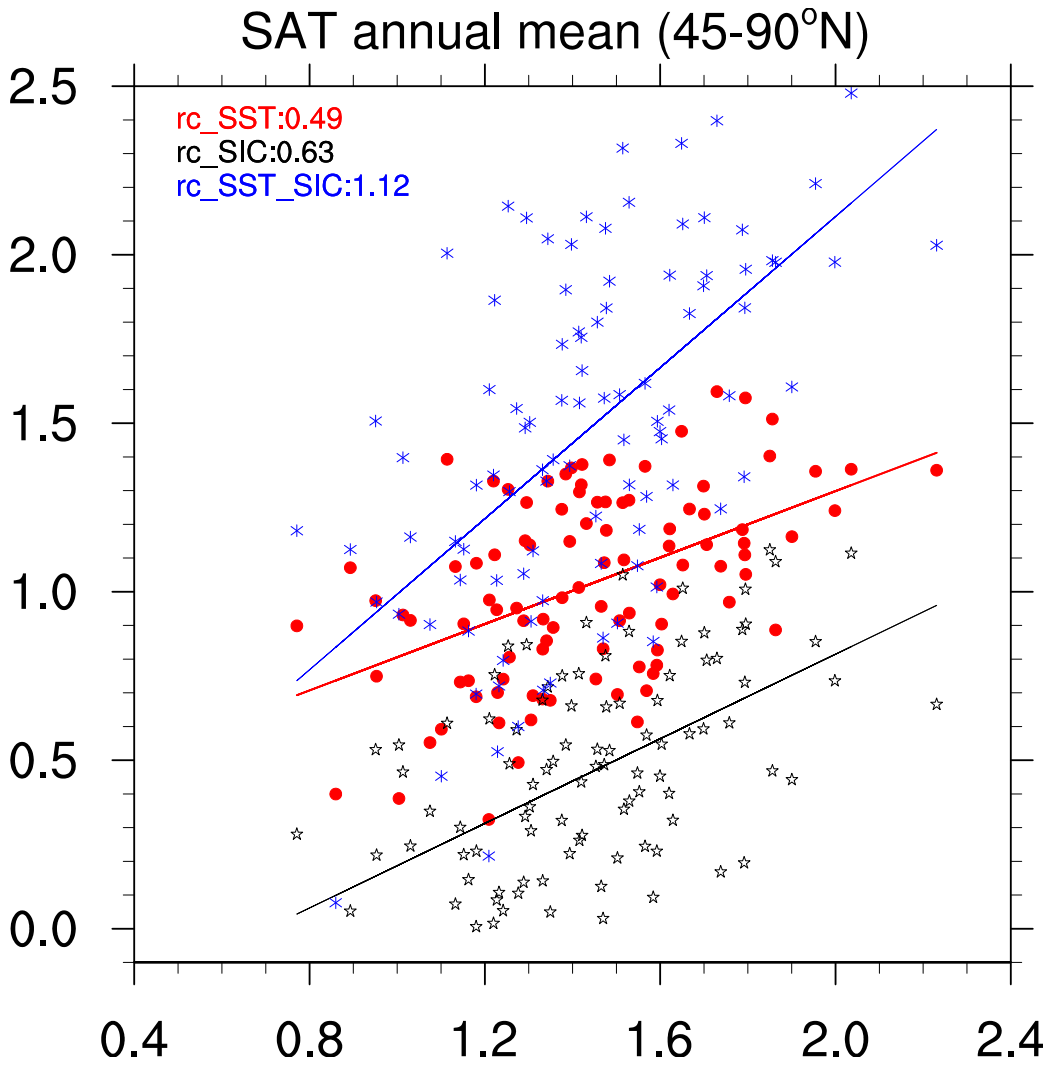

Fig. 13. Scatter plot of the annual mean SAT responses for the 45-90°N mean by

using the large-ensemble simulations of No.1.1 (pdSST-pdSIC), No.1.2 (piSST-piSIC), No.1.3 (piSST-pdSIC) and No.1.5 (pdSST-piArcSIC). The abscissa denotes SAT_{all} (pdSST-pdSIC minus piSST-piSIC), and the vertical coordinate denotes SAT_{sst} (pdSST-pdSIC minus piSST-pdSIC) for red dots, SAT_{Arc} (pdSST-pdSIC minus pdSST-piArcSIC) for black five-pointed stars, and SAT_{sum} (SAT_{sst} plus SAT_{Arc}) for blue asterisks. The linear regressions of SAT_{sst}, SAT_{Arc}, and SAT_{sum} on SAT_{all} are also represented by the regression lines in the corresponding colors. The regression coefficients are shown in the upper left corner.